Simulation Modelling Practice and Theory 149 (2026) 103279

Contents lists available at ScienceDirect

Simulation Modelling Practice and Theory

journal homepage: www.elsevier.com/locate/simpat

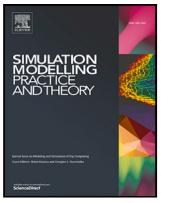

Modeling crowd flow during stadium ingress under alternative access protocols: San Mamés as a case study

Ander García [a,b,*], Bruno V. Guerrero [a,*], Dariel Hernández-Delfin [c], Dae-Jin Lee [d], Marco Ellero [a,e]

[a] BCAM - Basque Center for Applied Mathematics, Mazarredo, 14 E48009 Bilbao, Basque Country, Spain
[b] Department of Mathematics, University of the Basque Country UPV/EHU, P.O. Box 644, 48080 Bilbao, Spain
[c] Department of Civil and Environmental Engineering, Imperial College London, London SW7 2AZ, United Kingdom
[d] IE University - School of Science and Technology, Paseo de la Castellana 259, E-28029, Madrid, Spain
[e] IKERBASQUE, Basque Foundation for Science, Calle María Diaz de Haro 3, 48013 Bilbao, Spain

ARTICLE INFO

Keywords:
Pedestrian dynamics
Crowd management
Crowd safety
Social force model
Numerical simulation
Human safety

ABSTRACT

Mass gatherings at sporting events pose critical risk for crowd safety, especially in venues with limited history of hosting high-demand events or insufficient data to inform evidence-based interventions. Ahead of the UEFA Europa League (UEL) Final 2024–2025, San Mamés Stadium implemented staged access protocols across league matches. These real-world experiences provide a timely case study on crowd management strategies and operational planning in urban environments. This work presents a simulation-based study of the pedestrian ingress dynamics during fan entry to the stadium under high-attendance settings. The agent-based modeling framework integrates a Social Force Model that considers the pedestrian's limited visual range, queuing behavior, and where path-finding is computed from the numerical solution of the Laplace equation. Using empirical data of the geometrical constraints of the stadium and its surrounding areas and timestamped turnstile access records from pre-final league matches, the model reproduces the pedestrian flow under every access protocol implemented during the tournament. Quantitative analysis of ingress efficiency, access rates, and pedestrian flow patterns reveals specific stadium-adjacent zones susceptible to undesired counterflow and overcrowding. Simulations indicate that the suggested access guidelines can streamline crowd movement and lower density levels by roughly 20%, while delaying individual screening at the fenced security perimeter by 2.5 s can decrease the maximum average local density by nearly 80%. These findings emphasize the role of computational modeling as a decision-support tool, allowing the evaluation of alternative crowd management strategies before their implementation in real-world events.

1. Introduction

In recent years, major European cities and urban centers worldwide have shifted markedly towards pedestrian mobility. However, increasingly dense pedestrian-oriented urban spaces also bring new challenges related to the safe and efficient displacement of people, demanding a deeper understanding of pedestrian dynamics. Inefficient urban mobility planning and crowd management during large-scale events pose significant safety risks [1,2], as evidenced by fatalities during religious gatherings [3–6], festivals [7,8], and other large-scale celebrations [9,10].

* Corresponding authors at: BCAM - Basque Center for Applied Mathematics, Mazarredo, 14 E48009 Bilbao, Basque Country, Spain.
E-mail addresses: angarcia@bcamath.org (A. García), bguerrero@bcamath.org (B.V. Guerrero).

https://doi.org/10.1016/j.simpat.2026.103279
Received 2 December 2025; Received in revised form 23 February 2026; Accepted 17 March 2026
Available online 18 March 2026

Crowd disasters in sports venues have resulted in catastrophic fatalities, exemplified by Heysel (1985) [11] and Hillsborough (1989) [12] tragedies, which claimed 39 and 97 lives, respectively. Despite decades of progress in crowd safety, recent events continue to result in mass casualties: at least 125 deaths in Indonesia (2022) [13], 12 in El Salvador (2023) [14], and 56 in Guinea (2024) [15]. Even non-fatal incidents, such as the 2022 UEFA Champions League final at the Stade de France [16], demonstrate how failures in access management can produce life-threatening congestion and hazardous conditions. Collectively, these adverse incidents highlight the risks and severe consequences of inadequate ingress planning and the urgent need for reliable, evidence-based crowd management strategies.

Pedestrian dynamics, as an emerging multidisciplinary research field, has advanced substantially, providing a deeper understanding of both individual and collective behavior under diverse conditions. Studies based on experiments and real-world events, where pedestrians are video-tracked, have revealed fundamental relationships, such as the speed–density diagram [17–21], and helped to characterize collective phenomena, including pedestrian flow through bottlenecks [22–29], physiological and psychological factors influencing crowd behavior [30–33], as well as the macroscopic responses under high-density conditions [34,35]. Modeling approaches have progressed from the Social Force model [36] and subsequent force-based frameworks (e.g., [37–39]) to velocity and navigation-field models [40–42], hydrodynamic descriptions [43], time-to-collision [44] and anticipation based algorithms [45], cellular automata [46,47], and, more recently, developments combining theoretical interpretability and machine learning predictions [48]. In addition, hybrid and data-driven frameworks integrating game-theoretic reasoning, sensor feedback, and adaptive control [39,49,50] are gaining prominence and further contributing to enhancing realism in simulations and crowd management solutions. The following reviews by Duives, Haghani, Yang, Corbeta, Dang, and their respective collaborators [51–55] provide comprehensive overviews of the different approaches, discussing the strengths, limitations, and challenges of simulating high-density scenarios.

Research on crowd dynamics in stadiums has predominantly focused on pedestrian egress and evacuation, relying on modeling frameworks based on cellular automata, agent-based, and social force models [56]. In football-related studies with cellular automata, Klüpfel and Meyer-König [57] reproduced empirical flow–density relationships and defined local congestion above 4 person/m^2, Tsiftsis et al. [58] replicated observed mean velocities and outflow rates, Dong et al. [59] analyzed crowd dispersal beyond the venue, and Yang [60] highlighted how density-driven speed reductions and localized bottlenecks limit evacuation efficiency. Among agent-based modeling studies, Gravit et al. [61] compared the Roman Colosseum and Gazprom Arena, revealing that the ancient structure surprisingly allowed a more efficient egress, Fang et al. [62] incorporated route choice and queue dynamics to enhance outflow, and Chin et al. [63] validated movement profiles and exit decision models with empirical data.

In contrast, pedestrian ingress under high-demand conditions in large venues remains insufficiently understood, limiting reliable predictive modeling and proactive crowd management. Effective ingress management is crucial to prevent tragedies (such as those at Hillsborough, El Salvador, and the 2022 UEFA Champions League final), ensure operational throughput and contribute to the success of large-scale events. To the best of our knowledge, the contribution of García et al. [64] remains the only study offering an examination of stadium fan access, albeit restricted to a single grandstand and with the capacity restrictions due to COVID-19, while the broader literature on pedestrian dynamics provides only a partial understanding of crowd inflow dynamics.

To address this gap in understanding how massive crowds enter stadiums under real-world operational settings, the present work examines stadium-wide pedestrian ingress under the same ingress protocols implemented at San Mamés Stadium during the 2024–2025 UEFA Europa League (UEL) season. The study aims to assess the effectiveness of these access guidelines to advance understanding of crowd dynamics in real stadium environments, inform targeted measures to mitigate congestion risks, and support evidence-based decision-making for stadium management during high-capacity events.

The remainder of this paper is organized as follows. We first provide detailed information on the venue and describe the access protocols implemented during actual UEFA Europa League matches at San Mamés. Then, we present the simulation framework, including the empirical data (the actual geometrical configuration and turnstile log records) and the pedestrian dynamics model. Next, we simulate fan ingress from the surrounding streets towards the stadium and evaluate the effectiveness of each access protocol by examining entry rates, flow patterns, and local density maps. Finally, the results are discussed, and the main conclusions are summarized.

2. Methods and materials

2.1. Venue and operational context

San Mamés Stadium, home of Athletic Club in Bilbao, Spain, offers us an ideal urban setting for analyzing large-scale pedestrian influx in dense settings. Fig. 1 provides a Google Maps view, with the stadium gates labeled for reference.

Inaugurated in 2013 in Bilbao's urban core, San Mamés Stadium exemplifies a UEFA Category 4 (Elite) facility that adheres to highest international standards for safety and accessibility. It features a capacity of 53,289 all-seater spectators, multimodal transport connectivity (including metro, tram, bus, and pedestrianized streets) and multiple entry points with segregated zones for VIP and general admission spectators. While its architectural layout facilitates crowd circulation under high-demand conditions, it also adds complexity to pedestrian mobility patterns, thereby necessitating proactive, evidence-based crowd management solutions capable of supporting safe and adaptive operations during high-profile events.

This venue has hosted a wide list of high-profile sporting and cultural events. Notable sports matches include UEFA Champions League fixtures as the 2025 final [65], the 2018 European Rugby Champions Cup Finals [66], the 2024 UEFA Women's Champions League Final [67], top-tier professional fixtures from the Spanish leagues, including La Liga and the Copa del Rey, as well as

Fig. 1. Google Maps top view of San Mamés stadium and its surrounding streets, with access gates numbered.

international friendlies. Looking ahead, the stadium will host the European Rugby Finals again in 2026 [68] and Spain's matches up to the quarterfinals of the 2030 FIFA World Cup [69]. Beyond football, San Mamés has also hosted large-scale concerts, community events and civic gatherings, proving its versatility as a multifunctional urban venue.

During the 2024–25 UEFA Europa League (UEL) fixtures at San Mamés, the access protocol followed a progressive, risk-based escalation aligned with the operational complexity and significance of each event. The measures comprised barrier deployment, pre-assigned entry points and designated circulation routes for distinct supporter groups. Table 1 presents the corresponding access protocols, ordered numerically to reflect the security deployment.

At the baseline level, such as during domestic league fixtures under the standard access management (where The Camino de la Ventosa is generally not used as an access route), measures focus on standard control in each of the entry gates according to ticketing sectors.

As events gained international relevance, for the Athletic vs. Roma fixture was implemented a crowd management protocol separating home and away supporters. Segregation was achieved through physical barriers and the strategic deployment of Ertzaintza (Basque Police) along predefined routes. Away supporters were escorted from their fan zone to stadium gates 21 and 22, with Felipe Serrate Street and the zone from Sabino Arana Avenue to Gate 19 of San Mamés temporarily reserved exclusively for their access (see Fig. 1). Home supporters were advised to follow a clockwise circulation pattern aligned with their assigned entry gates. The access through Camino de la Ventosa was closed to spectators and reserved for logistical and operational purposes only.

For higher-risk Athletic matches, specifically those against Rangers and Manchester teams, the protocol enhanced security and incorporated a clockwise access to the stadium gates [70,71]. Segregation between away and home supporters was maintained. Gates 21 and 22 were reserved for away fans as during the match against Roma's team. Local supporters accessed the stadium via pre-designated routes to avoid crowding near the ticket offices (gates 7–13): gates 23–26 via Pozas-Briñas or Urquijo; gates 1–13 via Paseo Rafael Moreno 'Pitxitxi'; and gates 14–20 by descending from Paseo Pitxitxi to Camino de la Ventosa and walking around the stadium to reach their designated entry gates.

For the UEL Final, the highest-security event, the full scale protocol was implemented, including city-wide fan segregation from two Fan Meeting Points (Etxebarria Park and Amezola), international police coordination, and three security perimeters: (i) Sabino Arana Avenue for ticket checks and initial screening; (ii) the stadium's fenced perimeter at the concourse, restricted to ticket- and credential-holders; and (iii) entrance turnstiles for final access control to the stands. Access was segregated for safety, dividing the area adjacent to the stadium into two distinct zones [72]: Tottenham Hotspur fans used gates 1–6 and 21–26, while Manchester United supporters used gates 7–21 (as shown in Fig. 3).

Table 1
Hierarchical classification of the access guidelines and security protocols used at San Mamés Stadium (UEL 2024–25 season). For Protocol 3, the variants labeled with suffixes ".1" and ".2" denote the specific match (ATH versus RAN or TOT, respectively) but the crowd management protocol remains identical. Abbreviations: ATH (Athletic Club), ATL (Atlético de Madrid), ROM (AS Roma), RAN (Rangers), TOT (Tottenham Hotspur), MUN (Manchester United), UEL (UEFA Europa League).

Protocol label	Representative match	Context
1	ATH vs ATM (29 Feb 2024)	Copa Del Rey match with standard intervention Highest-attendance for a domestic match Absence of predefined access protocol
2	ATH vs ROM (13 Mar 2025)	UEL Round of 16. Away supporters escorted to gates 21 and 22 Locals with clockwise access and exclusion area
3.1	ATH vs RAN (17 Apr 2025)	UEL quarter-final Away supporters escorted to gates 21 and 22 Access guidelines for local supporters
3.2	ATH vs MUN (1 May 2025)	UEL semi-final. Large away support Away supporters escorted to gates 21 and 22 Access guidelines for local supporters
4	TOT vs MUN (21 May 2025)	UEL final. Neutral venue. City-wide segregation and additional security control at the fenced perimeter

For matches listed in Table 1, Athletic Club provided the complete turnstile entry records corresponding to the 24 authorized gates (gates 5 and 10 are restricted). The dataset does not include fans attending the VIP ring, which has a capacity of 2030 spectators. Additionally, for Protocols 2 and 3, away supporters were not considered in the simulation, since their entrance was managed under police escort via a segregated and restricted access corridor, isolating their movement from the regular spectators. The 1-min-resolution arrival time series record the precise moment each home supporter passed through a designated entry gate, supplying high-resolution empirical data for the analysis of real-world ingress dynamics at San Mamés Stadium.

2.2. Digitalized geometry of San Mamés

The San Mamés area, encompassing the stadium, its concourse, and the surrounding urban fabric, was digitally reconstructed for simulation purposes using architectural blueprints provided by Athletic Club authorities, supplemented with spatial projections from Google Earth to ensure accuracy.

Fig. 2 illustrates the geometric configuration implemented in the simulation model, encompassing the stadium and its authorized entry gates, the five designated access routes pedestrianized during match-days (relabeled in this work as Str. 1–5), and the deployment of mobile barriers used to manage pedestrian flow according to the operational protocols summarized in Table 1. Black segments denote permanent structural boundaries (i.e., solid walls common to all four protocols), whereas colored segments indicate protocol-specific simulated barriers. This distinction allows evaluation of adaptive access management strategies and their effects on pedestrian flow efficiency.

Our modeling framework considers the four distinct access protocols implemented during the UEL 2024–25 (see Table 1). For the numerical simulations, each protocol is implemented by selectively activating artificial "wall segments" (virtual constructs that restrict pedestrian movement in the simulation, irrespective of whether physical infrastructure was actually present during the real event). Protocol 1, illustrated in Fig. 2(a), enables all spawning streets and activates the red segments (virtual, with no physical counterpart) to block access to Camino de la Ventosa (blue area). In this scenario, agents are free to move throughout the geometry without restrictions. Protocol 2, sketched in Fig. 2(b), forbids spawning from Str. 1 and activates the green segment, which corresponds to a real barrier deployed during the events to achieve spatial segregation between home and away supporters. In this scenario, local fans are forced to walk clockwise around the stadium to reach gates 1–20. In addition, the closure of the blue area via the active red segments is maintained. Protocols 3, shown in Fig. 2(c), forbid spawning from Str. 1 and activate the green segment for all pedestrians, as in Protocol 2, to enforce home and away supporters' segregation. The remaining colored segments are activated or deactivated depending on pedestrians' target grandstands. For agents entering through the South and Main Grandstands (Gates 23–26 and 1–6), the red and purple segments are active. For fans accessing the North Grandstand (Gates 7–13), the red segments are active and the purple ones are inactive, enabling the light purple area beside the stadium. For East Grandstand supporters (Gates 14–20), the purple segments are activated and the red ones are inactive, redirecting the flow through Camino de la Ventosa (blue area). Finally, Protocol 4, depicted in Fig. 2(d), replicates the actual second security perimeter used during the UEL final. The five spawning areas are deactivated and replaced by discrete entry points, indicated by the blue lines. In addition, the virtual red segments blocking Camino de la Ventosa and the yellow segments corresponding to the actual fencing, its access doors, and excluded areas, according to on-site security measures, are activated.

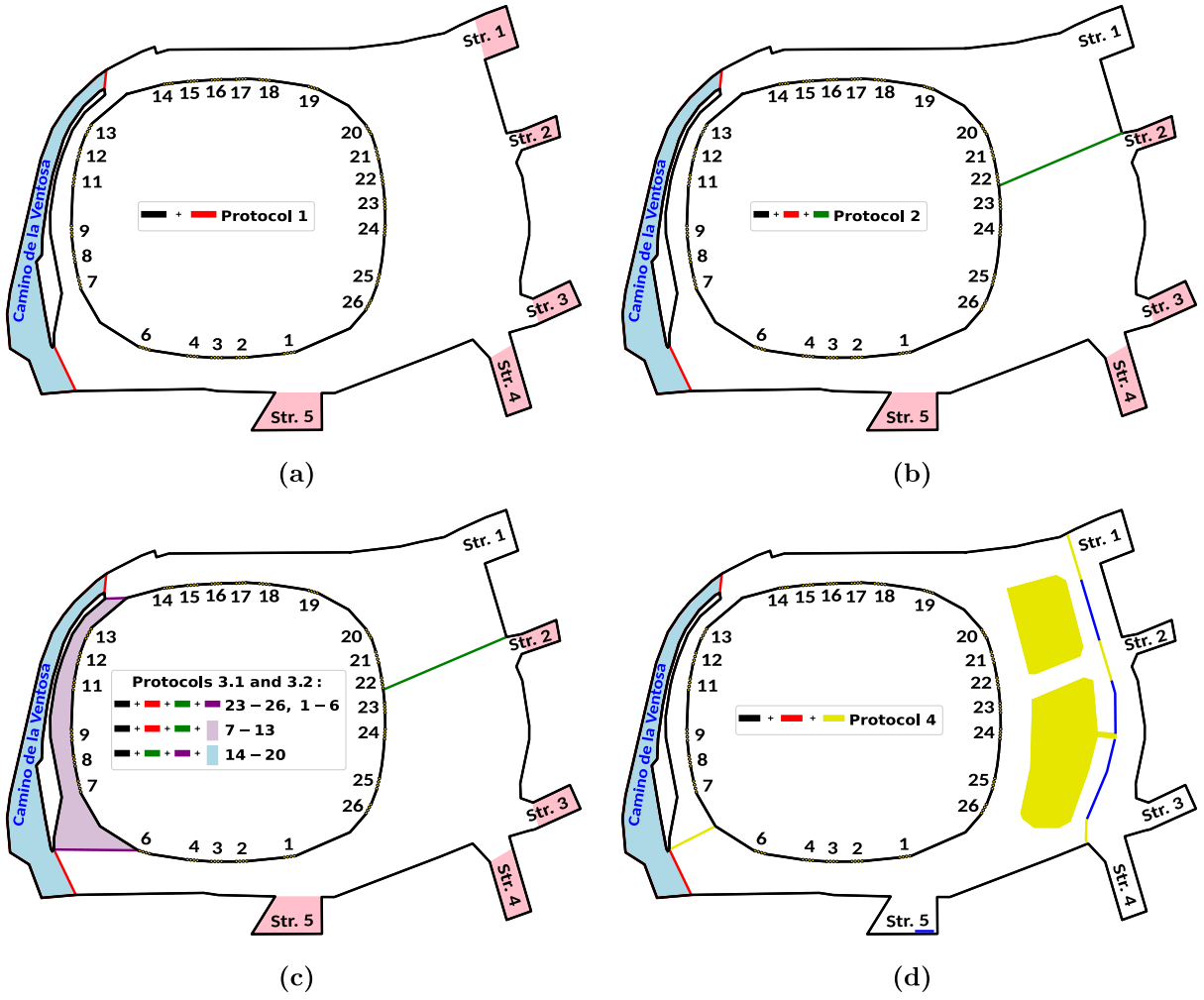

Fig. 2. Geometric configuration of the simulation, including the stadium, authorized entry gates, five spawning streets labeled as Str.1-5, and mobile barriers used to manage pedestrian flow according to the protocols: (a) 1, (b) 2, (c) 3.1 and 3.2, and (d) 4. Black segments denote permanent walls, while colored segments indicate protocol-specific simulated barriers.

2.3. Pedestrian dynamics simulation framework

Our simulation framework is built upon the same modified version of the Social Force Model (SFM) described in [37] equipped with pedestrians' limited visual range, the coupling of time-independent velocity fields as a path-finding strategy [64], and a queuing mechanism [73]. As formulated in the SFM of Helbing et al. [36,74,75], the equation of motion for each pedestrian i, out of a total of N with mass m, is governed by three force contributions:

$$m\frac{d\mathbf{v}_i(t)}{dt} = \mathbf{f}_i^{\mathrm{d}} + \sum_{j\neq i}^{N}\mathbf{f}_{ij}^{\mathrm{r}} + \sum_{j\neq i}^{N}\mathbf{f}_{ij}^{\mathrm{c}}, \tag{2.1}$$

where $\mathbf{f}_i^{\mathrm{d}}$ represents the driving force, $\mathbf{f}_{ij}^{\mathrm{r}}$ the social repulsive interactions, and $\mathbf{f}_{ij}^{\mathrm{c}}$ the contact forces.

The driving force, which establishes the intended movement direction and guides pedestrian i towards its target destination, is given by:

$$\mathbf{f}_i^{\mathrm{d}}(\mathbf{r}_i(t)) = m\frac{v_i^0\hat{\mathbf{e}}_i(\mathbf{r}_i(t)) - \mathbf{v}_i(t)}{\tau}, \tag{2.2}$$

where $\mathbf{v}_i(t)$ is its actual velocity at time t, v_i^0 the magnitude of its desired velocity, $\mathbf{e}_i$ is a unit vector defined in Section 3.1 which is oriented towards the desired target, and τ a characteristic time related to the relaxation time of the particle to achieve the desired speed.

The repulsive component of the force, $\mathbf{f}_{ij}^{\mathrm{r}}$, corresponds to interactions responsible for preventing physical collisions between agents and obstacles (either other surrounding pedestrians or wall particles). To model personal space and anticipatory avoidance behavior, we employ the asymmetric elliptical specification of the social force [37,64]

$$\mathbf{f}_{ij}^{\mathrm{r}} = w(\varphi_{ij}) \cdot A e^{-\frac{b_{ij}}{B}} \cdot \frac{\left\|\mathbf{r}_{ij}\right\| + \left\|\mathbf{r}_{ij} - \mathbf{y}_{ij}\right\|}{2b_{ij}} \cdot \frac{1}{2}\left(\hat{\mathbf{u}}_{ij} + \frac{\mathbf{r}_{ij} - \mathbf{y}_{ij}}{\left\|\mathbf{r}_{ij} - \mathbf{y}_{ij}\right\|}\right), \tag{2.3}$$

where A and B control interaction strength and range, respectively, $\|\mathbf{r}_{ij}(t)\| = \|\mathbf{r}_i(t) - \mathbf{r}_j(t)\|$ is the relative distance between pedestrian i and obstacle j at time t (pointing from j to i), in the direction of $\hat{\mathbf{u}}_{ij} = \frac{\mathbf{r}_{ij}}{\|\mathbf{r}_{ij}\|}$.

$$\mathbf{y}_{ij} = (\mathbf{v}_j - \mathbf{v}_i)\Delta T \tag{2.4}$$

is a vector associated with the anticipated relative displacement pointing from agent i to agent j (relative displacement) over an anticipation time ΔT, and

$$2b_{ij} = \sqrt{\left(\left\|\mathbf{r}_{ij}\right\| + \left\|\mathbf{r}_{ij} - \mathbf{y}_{ij}\right\|\right)^2 - \left\|\mathbf{y}_{ij}\right\|^2} \tag{2.5}$$

is the semi-minor axis of the ellipse. The role of limited visual range is included in social repulsive forces $\mathbf{f}_{ij}^{\mathrm{r}}$ by including the weight factor $w(\varphi_{ij})$ [75] that accounts for how strong a person reacts to the surrounding individuals according to their position within the visual field:

$$w(\varphi_{ij}) = \lambda + (1 - \lambda)\frac{1 + \cos(\varphi_{ij})}{2}, \tag{2.6}$$

where $\lambda \in [0, 1]$ and φ_{ij} is the angle between $\mathbf{v}_i$ and $\mathbf{r}_{ji} = -\mathbf{r}_{ij}$:

$$\cos\left(\varphi_{ij}\right) = \frac{\mathbf{v}_i}{\|\mathbf{v}_i\|} \cdot \frac{\mathbf{r}_{ji}}{\|\mathbf{r}_{ji}\|} \tag{2.7}$$

This weight factor results in social repulsive forces that do not conserve linear momentum (i.e., $\mathbf{f}_{ij}^{\mathrm{r}} \neq -\mathbf{f}_{ji}^{\mathrm{r}}$), since agents located in front of a reference agent i repel it more strongly than those behind it.

For pedestrian interactions with boundary particles, $w(\varphi_{ij}) = 1$ to neglect the asymmetrical contribution due to the limited visual range [37].

Finally, the contact force related term $\mathbf{f}_{ij}^{\mathrm{c}}$ includes short-range physical contact forces activated when their separation falls below the sum of their effective radii. Agents are represented as deformable (soft) disks with radii R_i and these forces are modeled as:

$$\mathbf{f}_{ij}^{\mathrm{c}}(\mathbf{r}_{ij}(t)) = H\left(R_{ij} - r_{ij}\right)\hat{\mathbf{u}}_{ij} + \gamma\left(R_{ij} - r_{ij}\right)\left(\mathbf{v}_{ji} \cdot \hat{\mathbf{t}}_{ij}\right)\hat{\mathbf{t}}_{ij}, \tag{2.8}$$

where H corresponds to the normal (compressive) stiffness associated with body compression under contact, and γ to the tangential (shear) damping coefficient. The relative velocity between agents is $\mathbf{v}_{ji} = \mathbf{v}_j - \mathbf{v}_i$, and the unit tangential vector is $\hat{\mathbf{t}}_{ij} = (-u_{ij}^2, u_{ij}^1)$.

Most of the model parameters are taken from our previous work [37]. For completeness, the values used in the present study are summarized in Table 2. The introduction of all mentioned phenomenological features into the modeling framework, together with the parametric choice reported in Table 2, allows to reproduce macroscopic empirical data (such as speed–density fundamental diagrams and pedestrian flow through bottlenecks), as well as lane pattern formation observed in bidirectional flows, and collision avoidance at the microscopic scale for low relative velocities, as addressed in [37].

Within this modeling framework, population size heterogeneity is introduced by assigning each agent a radius sampled from a Gaussian distribution with mean μ_R and standard deviation σ_R. This polydispersity captures bodies size variability that enhances the realism of the system and mitigate the nonphysical clogging artifacts often observed in homogeneous bidirectional pedestrian flow simulations [37]. The selected pedestrian sizes are comparable to reported in [41].

As in the extension of the Social Force Model presented in [73], we add this queuing mechanism at stadium entrances. Virtual nodes are located in the gates position (depicted as yellow dots in Fig. 3) as reference points from which queues will spontaneously develop. When an entrance is unoccupied, the first arriving pedestrian triggers queue formation once the distance to a virtual node is smaller than the queuing cutoff radium R_q. Subsequent agents will align with the queue if their separation from queuing individuals also falls below R_q. To ensure a realistic assignment, the selected gate must be consistent for both arriving and queuing pedestrians, preventing misallocation to unintended gates.

Once a pedestrian becomes part of a queue, its speed is slowed down and its social repulsion is lessened to reproduce empirically observed patterns of ordering and inter-personal spacing in real queues. This adaptation is achieved by reducing both the desired velocity and the intensity of the social repulsive force governing pedestrian interactions. Specifically, the average desired speed $\mu(v_i^0)$ and the social force intensity A are recalibrated as follows:

$$\begin{cases} v_Q^0 = c_q\, v_i^0, \\ A \to A_q, \end{cases} \tag{2.9}$$

being $c_q \in (0, 1]$ a scalar coefficient that reduces speed and v_Q^0 the reduced desired speed of pedestrians part of the queue, while the queuing social force intensity $A_q < A$ captures the diminished interpersonal tension typically observed among pedestrians once an

Table 2
Model parameters governing pedestrian behavior and their values in the simulations.

Parameter	Value	Description
m	80 kg	Effective mass of each pedestrian
A	60 N	Intensity of the social repulsive force
B	0.6 m	Characteristic distance of the social repulsive force
H	1.2×10^4 kg s^{-2}	Stiffness coefficient of the contact force
γ	1.5×10^4 kg m^{-1} s^{-1}	Tangential shear coefficient of the contact force
τ	1 s	Relaxation time to reach the desired velocity
ΔT	1.5 s	Anticipation time horizon of agents
λ	0.1	Weighting factor for anisotropy in pedestrian perception
μ_v	1.45 m/s	Mean of the desired walking speed
σ_v	0.23 m/s	Standard deviation of the desired walking speed
μ_R	0.175 m	Mean of pedestrian's effective radius
σ_R	2.551×10^{-2} m	Standard deviation of pedestrian's radius
R_q	1.25 m	Threshold radius triggering queuing behavior
A_Q	15 N ($A/4$)	Reduced social force intensity for queuing pedestrians
v_Q^0	0.36 m/s ($\mu_v/4$)	Mean queuing velocity of pedestrian
c_Q	0.25	Scalar that reduces the desired speed at the queue
δt	10^{-3} s	Integration time step

ordered line is established. In Appendix A, we provide a sensitivity analysis of both parameters, R_q and c_q, to explore the effect of these parameters on the simulation outcomes.

Turnstile access records indicate a throughput of approximately 15 individuals per minute, i.e., a mean inter-arrival time, Δt, of 4 seconds per local supporter. Using this empirical observation, the characteristic velocity v_Q^0 can be guessed by considering that each subsequent person in the queue requires approximately 4 s to access, covering a distance R_c, then the estimated velocity would be roughly:

$$v_Q^0 \approx \frac{R_c}{\Delta t} = \frac{1.25 \text{ m}}{4 \text{ s}} \approx 0.31 \text{ m/s}.$$

in close agreement with the selected value $v_Q^0 = 0.36$ m/s from our previous study [73] (see Table 2).

3. Numerical implementation

Using the simulation modeling framework and the digitalized geometry of the venue, we proceed with the numerical implementation.

Boundary conditions are defined to reflect the physical constraints of the venue. Entrance gates and their turnstiles act as inflow boundaries, while access streets are modeled as outflow boundaries. Obstacles and walls are implemented as fixed, non-permeable boundaries, made of particles of radius $R_w = 0.5$ m, constraining pedestrians to their intended walkable areas.

Each pedestrian is represented as an autonomous agent initialized within designated spawning zones in Streets 1–5 (red colored areas in Fig. 2), and instantiated at its empirically observed turnstile access timestamp.

Accordingly, the simulation's reference time $t = 0$ s (taken when the first fan is created in any of the streets) is shifted relative to the real-world timeline by approximately the free-flow walking duration between each spawning location and its corresponding stadium gate. This offset is intentionally left uncorrected to preserve empirical fidelity, acknowledging that real walking times cannot be predetermined. Under crowded conditions, significant path deviations and clogging effects can increase the effective travel times beyond the free-flow estimates. While the omission of this offset may slightly bias the temporal alignment of pedestrian generation across gates, it does not affect the macroscopic flow dynamics or the validity of the model's findings.

In the absence of empirical data, as a tractable approximation of spatial distribution, each entering pedestrian is allocated to a specific spawning area based on the following synthetic probabilities:

- *Protocol 1:* 15% in Str. 1 (assumed lower because is not connected with metro or train stations), 22.5% in Str. 2, 40% in the intersection of Str. 3 and Str. 4 (20% each), and 22.5% in Str. 5.
- *Protocol 2:* 0% (because it is restricted to away supporters only) in Str. 1, and 25% in each of the other four streets.
- *Protocols 3:* the probabilities and spawning areas depends on their grandstand:
  - For home supporters entering the south (gates 23–26) and main grandstands (gates 1–6): 0% in Str. 1 and Str. 5, 50% in Str. 2, and 25% each in Str. 3 and Str. 4.
  - For home supporters entering the north (gates 7–13) and east (gates 14–20) grandstands: 0% in Str. 1 and Str. 2, 25% each in Str. 3 and Str. 4, and the remaining 50% from Str. 5.
- *Protocol 4:* Agents are spawned at discrete points at the fence's doors, separated according their supporting team.

These assumed probabilities encode assumptions about demand, accessibility, and behavioral heterogeneity that shape the spatio-temporal inflow patterns. To assess whether the numerical outcomes remain consistent under varying probability assumptions, Appendix B includes additional simulations in which agent generation distribution is varied across each available street. Future studies could leverage additional data sources, including video-based pedestrian tracking, to reconstruct trajectories prior to stadium entry. This would allow for a more precise mapping between street-level arrival times and turnstile access, as well as for the refinement of the temporal allocation of agents to their corresponding spawning locations.

3.1. Desired velocity field

Rather than recalculating each pedestrian's optimal direction $\mathbf{e}_i(\mathbf{r}_i(t))$ for every time instant, time-independent velocity fields are precomputed to encode the assumed optimal navigation pathways through the spatial domain [76]. This approach guides pedestrians along predefined routes, significantly reducing computational costs by avoiding real-time pathfinding for each agent.

The unit vectors $\mathbf{e}(\mathbf{r})$ define the orientation of the desired velocity field at each spatial position r and are given by:

$$\hat{\mathbf{e}}(\mathbf{r}) = \frac{\boldsymbol{\nabla} \mathcal{U}(\mathbf{r})}{|\boldsymbol{\nabla} \mathcal{U}(\mathbf{r})|}, \tag{3.1}$$

where $\mathcal{U}(\mathbf{r})$ is the solution to Laplace's equation, $\Delta \mathcal{U}(\mathbf{r}) = 0$, in a given domain Σ. Inlets in the geometry are prescribed with Dirichlet boundary conditions, $\mathcal{U}(\mathbf{r})\big|_{\mathbf{r}\in\partial\text{inlet}} = 0$, whereas outlets are assigned $\mathcal{U}(\mathbf{r})\big|_{\mathbf{r}\in\partial\text{outlet}} = 1$. Neumann boundary conditions are applied along walls and obstacles (walls represented with black lines in Fig. 2, including activated segments according to the applied protocol), expressed as $\nabla \mathcal{U}(\mathbf{r}) \cdot \hat{\mathbf{n}} = 0$, where $\hat{\mathbf{n}}$ is the outward-pointing normal vector to the surfaces. This generates a velocity field normal to the inlet and outlets and tangential to the walls, as illustrated in Fig. 3.

In our simulations, time integration is performed with a fixed time step $\delta t = 10^{-3}$ s and the spatial domain of the vector fields is discretized using a grid spacing of 0.25 m, sufficient to resolve the velocity fields and enable proper tracking of each pedestrian, while keeping the memory usage within our computational limits.

In contrast to our earlier work [64], which relied on a single desired velocity field towards a single grandstand, the current framework generates distinct velocity fields, one for each stadium gate and its corresponding street access route. The calculations of such fields are explicitly conditioned on the active crowd management protocol, by enabling or disabling the corresponding colored wall segments (see Fig. 2) to reflect real-world access restrictions through physical barriers and segregated pathways. For instance, Fig. 3(a) shows the desired velocity field for pedestrians spawned in Str. 2 and directed towards Gate 19 (descending by Camino de la Ventosa), following the access guidelines defined by Protocol 3.

For the UEL Final's match, outflow boundary conditions were imposed directly at the fenced security perimeter rather than at the surrounding street-level access points. As shown in Fig. 3(b), two distinct desired velocity fields were computed, one for each segregated supporter zone (blue and red, respectively). The blue streamlines represent pedestrian guidance from the perimeter inlets in the blue part of the fence to Gate 6, while the red streamlines depict flow from the inlets in the red part of the fence to Gate 7, illustrating the spatial segregation of the fan groups through gate-specific velocity fields.

The adoption of street- and gate-specific individual desired velocity fields (computed for each feasible street–gate pairing) is grounded in a behavioral hypothesis: pedestrians use their knowledge through prior experience (e.g., habitual or recommended routes) but generally lack global awareness of the entire entrance network. As a result, a local supporter going towards their designated gate cannot anticipate how alternative routes available elsewhere might influence their own flow patterns. This cognitive limitation justifies the assumption and implementation of multi-layered route-specific velocity fields instead of imposing a single global one.

The choice of these time-independent velocity fields favors computational efficiency and ensures that the exact same number of agents enters through each gate, as determined by turnstile data. Nevertheless, this comes at the expense of partially neglecting randomness at the tactical level, since agents do not avoid congested routes. Even in open areas or wide corridors, agents may traverse higher-density zones rather than detouring, as the predefined velocity map enforces preferred pathways, potentially overestimating local densities.

3.2. Calculation of the mean density field

Pedestrian facility design has long been grounded in fluid-dynamic analogies, using macroscopic descriptors such as density to quantify the level of crowdedness and to assess safety and level of service. The conventional definition, ρ = population/area, may become unreliable in capturing the discrete nature of pedestrian crowds. Recent studies [77,78] propose refined quantitative measurements that better capture fine-scale spatial variability and transient fluctuations in density, thereby extending the applicability of macroscopic metrics to regimes where continuum assumptions no longer hold.

In this work, to produce a smooth representation of density fields while capturing local fluctuations arising from inter-human interactions and geometrical constraints, the local pedestrian density, $\rho(\mathbf{r}_i)$, is evaluated on a regular mesh using the quantic spline kernel-based estimator commonly employed in smoothed-particle hydrodynamics (SPH) [79,80]:

$$\rho(\mathbf{r}) = \sum_{j\in\text{pedestrian}} W\left(\|\mathbf{r}_i - \mathbf{r}_j\|\right), \tag{3.2}$$

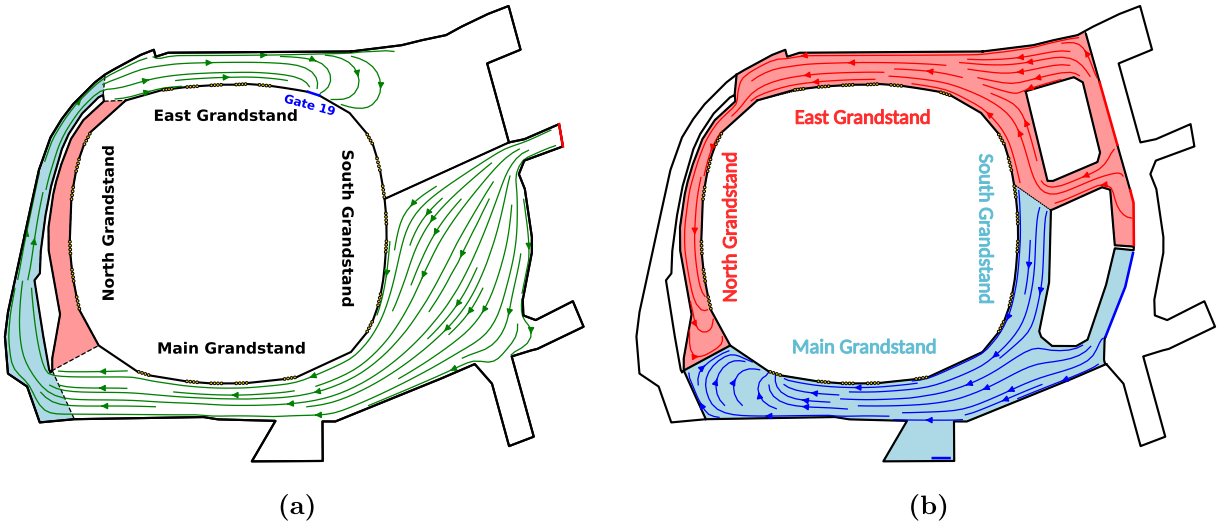

Fig. 3. Examples of desired velocity fields computed for San Mamés Stadium: (a) Starting from Str. 2 and directed towards Gate 19, following Protocol 3, which forces agents to use the blue-colored zone to reach the East Grandstand. (b) Showing route guidance from the security perimeter to Gates 6 and 7, respectively the blue and red colored zones denote the stadium sectors officially allocated to Tottenham Hotspur and Manchester United supporters, in accordance with event-specific spatial separation. In (a) and (b), black lines denote the boundaries where Neumann boundary conditions are applied.

where $W\left(\|\mathbf{r}_i - \mathbf{r}_j\|\right) \equiv W(r_{ij})$ is the piecewise-quintic smoothing kernel:

$$W(r_{ij}) = W_0 \times \begin{cases} \left(3 - \frac{r_{ij}}{h}\right)^5 - 6\left(2 - \frac{r_{ij}}{h}\right)^5 + 15\left(1 - \frac{r_{ij}}{h}\right)^5 & \text{if } 0 \le \frac{r_{ij}}{h} < 1 \\ \left(3 - \frac{r_{ij}}{h}\right)^5 - 6\left(2 - \frac{r_{ij}}{h}\right)^5 & \text{if } 1 \le \frac{r_{ij}}{h} < 2 \\ \left(3 - \frac{r_{ij}}{h}\right)^5 & \text{if } 2 \le \frac{r_{ij}}{h} < 3 \\ 0 & \text{if } \frac{r_{ij}}{h} > 3 \end{cases} \tag{3.3}$$

and h is the smoothing length that determines the supporting area of the smoothing function and $W_0 = 7/(478\pi h^2)$.

The mean density field, $\langle \rho(\mathbf{r}) \rangle$, is computed by time-averaging over all frames within a 15-minute period and across three independent realizations generated from different random seeds, to reduce stochastic variability and capture the spatio-temporal patterns. The resulting mean density field was then interpolated and plotted as heatmaps on a logarithmic scale, allowing better visual contrast between regions with lower and higher density levels.

4. Results

To complement empirical observations, agent-based simulations were used to explore pedestrian mobility patterns across multiple ingress protocols, capturing the dynamics of home supporters entering the stadium. The numerical simulations allow the identification of temporal clustering, possible gate-level bottlenecks, queuing and flow patterns that would be difficult to quantify from empirical arrival data alone.

This section focuses on macroscopic validation by comparing empirical and numerical arrival-time statistics and the identification of expected congestion patterns in terms of density heatmaps. Due to the lack of additional empirical data, the observed microscopic behaviors (queue shapes and localized high-density areas) are treated as predictive outcomes of the model. Each simulation was executed three times with independent random number generator seeds to account for the stochastic nature of pedestrian behavior. Averaging across these realizations reduced the influence of rare individual deviations, providing a reproducible characterization of collective crowd dynamics.

4.1. Arrival patterns and gate-level ingress

For those UEFA Europa League 2025–26 events analyzed in the present work, full-stadium entry data is available, capturing nearly 50,000 attendees across all grandstands. In contrast, our initial study [64] (where 15 fixtures during the 2021–2022 season were analyzed) was constrained by post–COVID-19 restrictions to 50%–85% of stadium capacity, with data available from roughly 5300 spectators of a single grandstand (representing a 10% of the stadium capacity). The complete arrival records, together with

Table 3
Total number of home supporters in each grandstand (excluding those in VIP zone) and in the stadium for the Athletic Club matches against Atlético Madrid, AS Roma, Glasgow Rangers, and Manchester United.

Protocol	Match	Main	North	East	South	Total
Prot. 1	ATH vs ATL	12 279	11 996	12 774	11 972	49 021
Prot. 2	ATH vs ROM	12 314	12 032	12 882	10 475	47 703
Prot. 3.1	ATH vs RAN	12 394	12 056	12 917	11 739	49 106
Prot. 3.2	ATH vs MUN	12 360	12 092	12 931	11 392	48 775

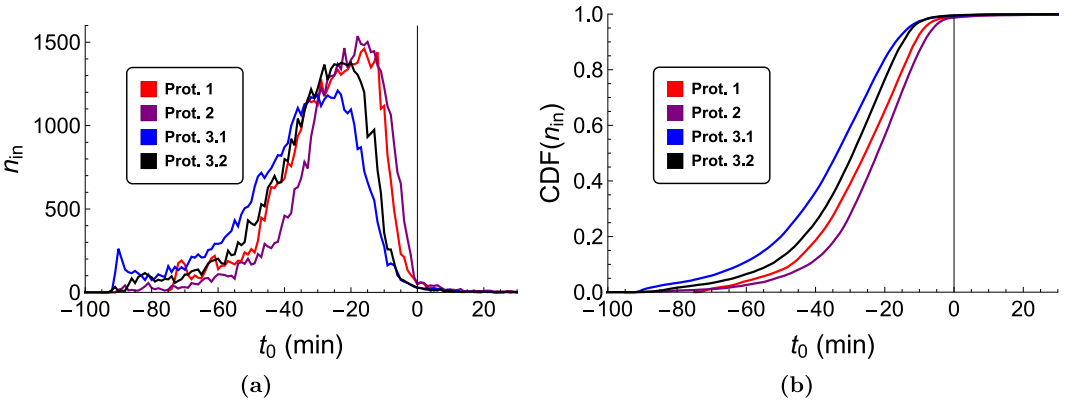

Fig. 4. For the matches listed in Table 1: (a) Empirical distribution of spectator arrivals over time, and its associated (b) cumulative distribution function.

the absence of social distancing measures, now enable a comprehensive characterization of crowd dynamics, capturing spectators' arrival patterns across the entire stadium during periods of high attendance.

Analysis of 1-min-resolution empirical arrival time series reveals that attendance levels approached the stadium capacity for all matches listed in Table 3. The sustained and relatively uniform high occupancy enables a preliminary evaluation of how differences in the venue layout and management strategies can influence crowd behavior in terms of arrival patterns at stadium gates.

At first glance, the total occupancy across the four grandstands (excluding the VIP zone) revealed consistent spatial asymmetries: the East Grandstand recorded the highest total occupancy, followed by the Main, North, and South grandstands. This result confirms the non-uniform distribution of attendees, with the East Grandstand having approximately 13% greater occupancy than the South Grandstand. It worth noticing that in cases with Prot. 2 and 3 about 2000 international supporters were referred to gates 21 and 22 and therefore are not considered.

Beyond the occupancy disparities linked to the facility's configuration, routing choices and seating allocation, fan arrivals are likely influenced by additional factors such as gate proximity and the spatial distribution of amenities, but the present data cannot confirm the underlying reasons. Further hypotheses concerning the causes of this heterogeneity would benefit from supplementary data, particularly on video recordings and pedestrian trajectories (both in the surrounding areas and intra-facility).

Subsequently, turnstile access data is analyzed, encompassing all 24 entry gates available for those matches outlined in Table 1. Fig. 4 illustrates the temporal evolution of spectators' arrivals, in terms of $n_{in}(t)$ (total number of spectators entering between t and $t+1$ min), and its corresponding cumulative distribution function, CDF(n_{in}), providing insight into the pace and distribution of ingress flows throughout the pre-event period.

The empirical entry-time distributions are strongly right-skewed and dispersed, with most spectators entering 10–30 min before kick-off. Early arrivals are sparse, followed by a sharp inflow peak, reflecting a common tendency to linger in nearby bars and public spaces until just before the event begins. Identifying the peaks in the arrival times provides actionable insights for proactive gate-level operational strategies: targeted staff allocation, ticketing and control protocols, adaptive queue management, staggered entry schemes, in order to mitigate congested access and preserve fans safety and comfort.

Compared to standard domestic matches [64], the arrival time distribution is broader in these UEL fixtures, consistent with record-attendance expectations. Moreover, the proportion of spectators arriving after $t_0 = 0$ min (kick-off time) is lower, indicating heightened punctuality and reflecting the event's perceived significance on spectator behavior.

Fig. 5 presents a comparison between the empirical (measured from turnstile data) and simulated entry times, in terms of n_{in} and their cumulative sums, N_{in}, for the full stadium under Protocols 1, 2, 3.1, and 3.2. For alignment with the empirical cumulative arrival-time functions, the numerical curves are time-shifted by the mean entry time of all agents (3.75 min for Prot. 1, 5.17 min for Prot. 2, 4.74 min for Prot. 3.1, and 4.81 min for Prot. 3.2).

The model's arrival distributions and their cumulative functions show a strong agreement with data, accurately capturing access patterns during those highest-attendance events irrespective of the crowd management strategy employed. In the cumulative functions, a significant bottleneck or clogging event would produce detectable delays (e.g., plateaus or reduced slopes in the

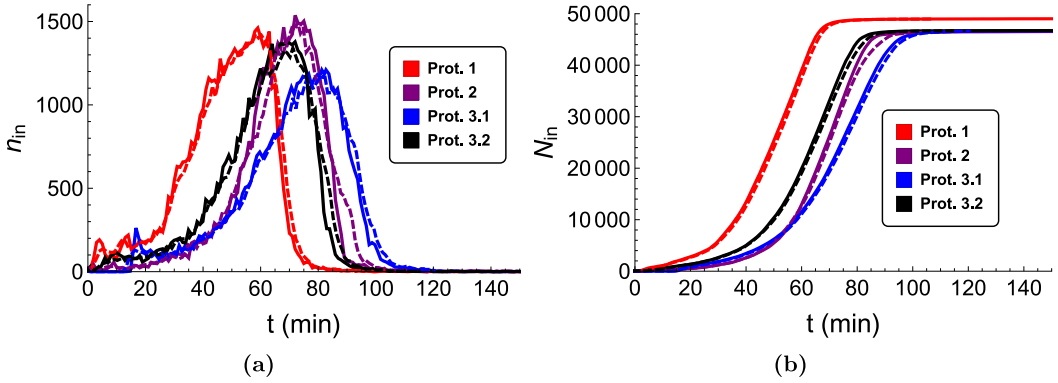

Fig. 5. Empirical (solid lines) and simulated (dashed lines) numbers of fans entering San Mamés Stadium relative to the first arrival time, for the matches listed in Table 1. (a) Distribution of spectator arrivals over time, and (b) its cumulative sum.

cumulative curve). The close agreement between empirical and simulated curves confirms that crowd access proceeded smoothly (without notable interruptions), as occurred in practice.

In line with our previous work, which involved a smaller-scale test at the Low-East grandstand of San Mamés Stadium [64] during the post-COVID-19 period, the current simulations successfully reproduce arrival dynamics from surrounding streets, offering further validation of both the modeling framework and parameter selection.

4.2. Local density fields

To identify potential congestion zones and corridor segments susceptible to bottlenecks, we examine the mean local density fields derived from the numerical simulations, as described in Section 3.2.

4.2.1. Impact of access protocols on crowd dynamics

For the matches listed in Table 1 with protocols 1–3, for which empirical arrival-time data are available, we compared their averaged density maps, generated using realistic access protocols and calibrated generation-time distributions derived from real-world arrival patterns.

Fig. 6 displays the averaged local density fields corresponding to the 15-minute interval of maximum congestion for the four crowd management protocols.

For simulations of domestic match-like settings, with baseline conditions without active crowd management, density heatmap (see Fig. 6(a)) indicates that the most critical congestion occurs in front of the North Grandstand (gates 7–13). The geometry of this corridor, combined with the accumulation of fans undergoing checks at gates 11 and 12, promotes bidirectional flows and localized overcrowding, identifying this narrow area as the highest-risk zone in this scenario. Despite this, for the selected queuing parameters, the peak values in the averaged density field remain around 0.75 person/m^{-2}, which does not exceed safety thresholds. Still, with a different parameter choice, this corridor is prone to overcrowding and clogging, as shown in Appendix A.

Under Protocol 2, Fig. 6(b), the barrier segregating visiting supporters disrupts bidirectional pedestrian flow for home supporters (only clockwise movement is possible) and the restricted access to Camino de la Ventosa forces spectators with assigned gates 14–20 to funnel through the narrow corridor adjacent to the north grandstand. As a result, Protocol 2 increases the average density exceeding 3 person/m^{-2} (with short periods of flow interruption), prone to overcrowding and potential incidents.

In Protocol 3, routing spectators via Camino de la Ventosa (for those heading to the East Grandstand) yields the safest and smoothest flow conditions, in comparison with the other two protocols. In Fig. 6 (c–d), heatmaps confirm that this approach effectively mitigates the severe congestion previously observed in the north grandstand corridor when Protocol 2 is applied. Two zones of comparatively low crowd density stand out: at the end of the detour (near gates 13 and 14) and in front of the Main Grandstand (gates 1–6). However, these are not congestion hotpots but rather areas of higher spectator affluence that do not represent a security threat.

Protocols 3.1 and 3.2's matches have a similar attendance level (see Table 3) but with differing arrival times (see Fig. 4(a)). The maximum local densities in the average density field are approximately 0.55 person/m^2 in Protocol 3.1 and 0.65 person/m^2 in Protocol 3.2, representing an 18% increase. Nevertheless, this crowd management intervention produces the safest overall scenario due to the segregation of pedestrian flow.

Within the considered parameter choice, no bottleneck was observed regardless the protocol but only zones with moderately higher density and continuous flow, as shown by the cumulative entry time curves and further justified in Appendix A.

In order to visualize the dynamics of the ingress process, Fig. 7 shows the density maps computed every 15-minute. The plots highlight the dynamical formation of localized aggregations while smoothing transient fluctuations. In the simulation, agents move continuously without voluntary pauses, unlike real individuals who may stop to wait for friends, take photos, or engage in other

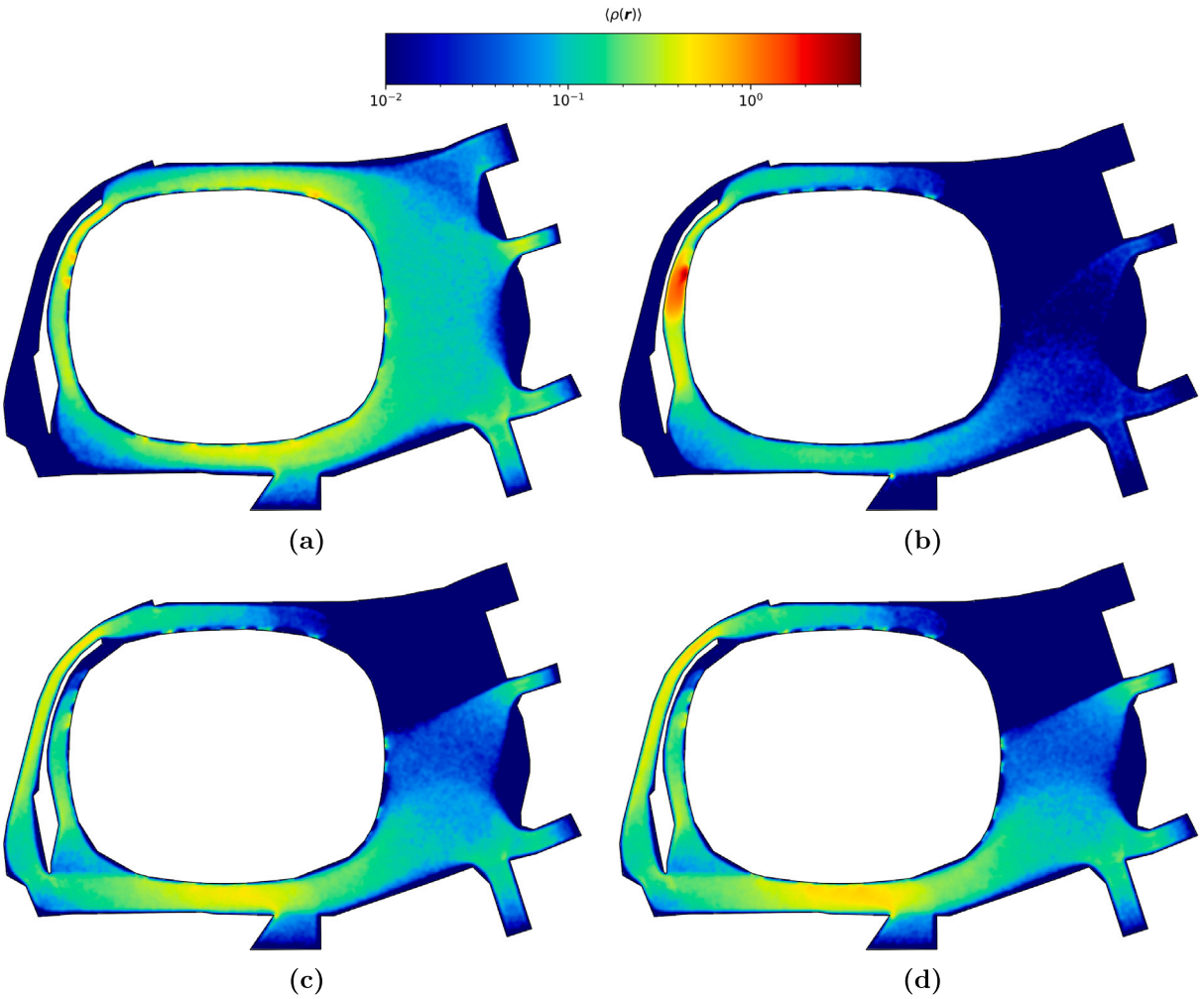

Fig. 6. Mean pedestrian density field $\langle\rho(\mathbf{r})\rangle$ in the 15 min with highest local density in the simulations of (a) Protocol 1 (b) Protocol 2, (c) Protocol 3.1, and (d) Protocol 3.2.

activities. Despite this simplification, the simulated dynamics reproduce the empirical access records and provide insights into how different access protocols influence flow patterns, illustrating how individual-based interactions and imposed geometrical constraints collectively shape crowd movement in real high-attendance events.

Notably, averaged local densities in our simulations ranged from 0 to 3.5 pers/m^2, remaining well below critical crowd thresholds [81], as illustrated by the color-scale of Fig. 7. This outcome aligns with the absence of reported crowd management incidents and further supports that our modeling framework can reliably reproduce real-life scenarios under normal conditions. Although local peak densities may slightly exceed these smoothed values, the mean densities provide a robust basis for assessing overall crowd dynamics and informing crowd management strategies.

4.2.2. Role of Fence's entry rates on flow patterns

During the UEL final, the city-wide crowd management protocol, labeled as Protocol 4, operated under conditions that prevent direct comparison with the other protocols. Within the modeling framework, the main difference lies in the presence of the fenced perimeter at the stadium concourse that channels spectators with entry rates governed by the throughput of the secondary screening.

As illustrated with the desired velocity field observed in Fig. 3(b), we simulate pedestrian flow through the fenced security checkpoint surrounding the stadium, by replacing the street spawning areas with 46 discrete spawning points in each zone.

Due to the lack of turnstile data, 50,000 agents are dynamically introduced at these points every 5, 7.5, or 10 s, corresponding to high, intermediate, and low flow rates. The duration of the security check was calibrated based on live recording evidence published by the sports newspaper Diario AS [82]. Manual inspection of the video (29:29–29:36 s) shows that individual security screenings last approximately 7 s, although the duration clearly fluctuates across pedestrians. We therefore adopt 7.5 s as a reference time.

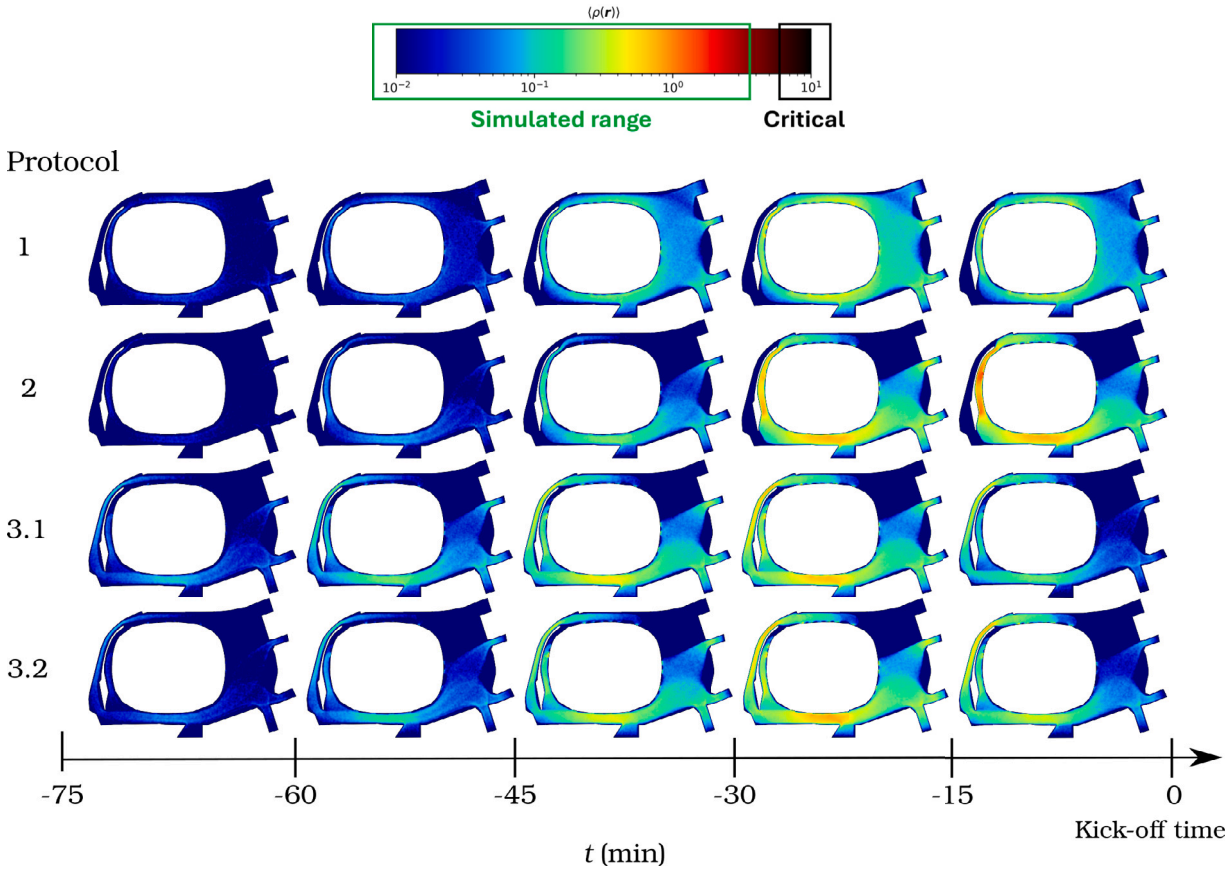

Fig. 7. Mean density fields, $\langle \rho(\mathbf{r}) \rangle$, computed in 15-minute windows from kick-off, for the protocols 1–3 outlined in Table 1. The colorbar indicates the density values in the simulated events and the critical density region [81].

Since inspection time enters the model as a service-rate parameter, our analysis focuses on the system-level sensitivity of the access rate to variations in this timescale rather than reproducing the full stochastic variability of individual checks. In real life, these screening intervals would correspond to quick ticket checks, (5 s/person), slower checks (7.5 s/person), or pat-down searches (10 s/person). With 46 spawning points per zone, this results in pedestrian inflows of 552, 368, and 276 people per minute in each zone. Fig. 8 shows the resulting average density fields from simulations at these three constant access rates (high, intermediate, and low, respectively) through the fenced perimeter.

Given that the spatial layout and movement protocols are identical across all three configurations, the principal zones of high pedestrian density are consistent. The first zone, adjacent to the north grandstand (discussed in Section 4.2), is driven by a combination of the geometrical constraint, high pedestrian flow, and queuing at the entrance gates. The second arises beside the large restricted zone on the San Mamés concourse (used as delivery and pickup areas), adjacent to the spawning points, highlighting how new possible areas prone to bottlenecks may emerge when geometry is changed with mobile obstacles.

Averaged local density values are strongly influenced by the inflow rate of agents: even small delays of 2.5–5.0 s per individual can significantly reduce the congested areas. In the high-flow scenario from Fig. 8(a), the highest values of local densities reach approximately 2.50 person/m^{-2} beside the north grandstand, and 3.60 person/m^2 around the large obstacle below the spawning points. For the intermediate-flow scenario in Fig. 8(b), the corresponding values are 0.49 person/m^2 (an 80% reduction relative to the high-flow case) and 1.44 person/m^2 (60% reduction), respectively. Finally, in the low-flow scenario shown in Fig. 8(c), densities decrease further to 0.39 person/m^2 (85% reduction) and 1.03 person/m^2 (71% reduction), respectively.

The analysis corroborates that, even under the same operational conditions, overcrowding in critical areas can be effectively alleviated by strategically delaying entry at external access checkpoints, such as those in the fenced perimeter or the outer security perimeter in Sabino Arana Avenue.

5. Discussion and conclusion

In the absence of comprehensive empirical datasets to calibrate and validate more advanced crowd models, this study provides a baseline simulation-based quantitative assessment of the risk-escalated crowd management protocols adopted during the UEFA

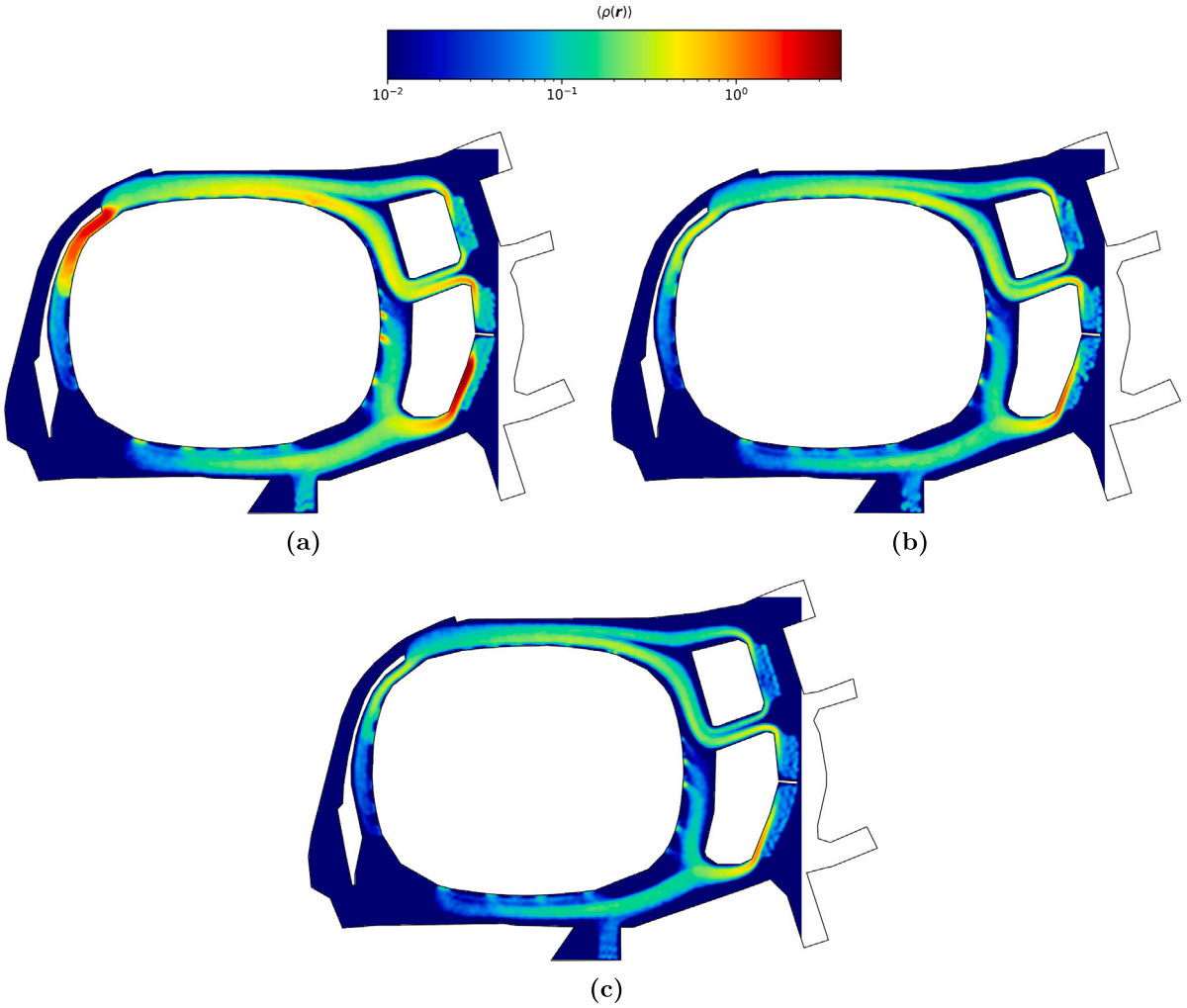

Fig. 8. Mean pedestrian density field $\langle \rho(\mathbf{r}) \rangle$ with the configuration of Protocol 4 considering (a) high inflow, (b) intermediate inflow, and (c) low inflow.

Europa League 2024–25 at San Mamés, contributing to understanding how the adopted measures have influenced the observed pedestrian dynamics and safety outcomes.

Based solely on the access data and the real geometry of San Mamés, we studied the complete stadium's filling process, considering all the actual crowd management protocols employed during the 2024–2025 UEFA Europa League. Pedestrian dynamics around the stadium were simulated using a calibrated social force model coupled with a static path-finding strategy (based on the desired velocity vector fields), limited range vision and queuing mechanism. Turnstile data from four high-attendance matches were used to dynamically generate agents into the simulation based on real events, and for the UEL Final fixture, different ingress rates were tested.

Empirical fan access to the entire venue was fairly replicated across all crowd management protocols. Based on these simulation outcomes, we constructed time-averaged density fields to quantitatively identify the potentially risky areas in the stadium surroundings. These protocol-dependent areas were localized especially in not-so-narrow corridors where bidirectional flows and interactions between queuing and non-queuing pedestrians occurred. The numerical results confirm the empirical findings observed in the actual real matches: Camino de la Ventosa as the detour route effectively reduces overcrowding in front of ticketing sectors at North Grandstand, producing the safest overall conditions.

Finally, the security perimeter employed during the UEFA Europa League Final was evaluated. By dynamically spawning pedestrians at discrete points to mimic access through the fenced security checkpoint, we studied the effect of high, intermediate, and low access rates on the density fields in the areas designated for Manchester United and Tottenham Hotspur supporters. Our simulations qualitative allow us to determine those zones with higher density and quantify the density reduction as delays in the security screening at the fence are introduced (particularly, delays of 2.5 and 5.0 s per individual, relative to the faster scenario).

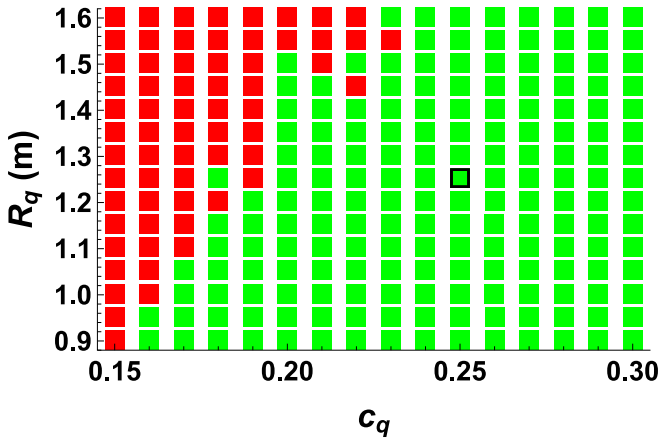

Fig. 9. Flow-clog diagram as a function of queuing parameters. Red squares indicate clog states and green squares free-flow states. The black contour square marks the parameter set employed in the main article.

The use of the desired velocity field as a path-finding strategy is a simplified representation of pedestrian decision-making within the modeling framework. While this have proven to be a convenient hypothesis for effectively capturing the aggregated pedestrian flows in high-attendance events (with limited empirical data), this assumption limits the model's capacity to reproduce unconstrained stochastic individual trajectories in less congested settings. As a result of this inability of simulated agents to detour in the presence of congested zones, the averaged density fields may tend to slightly overestimate the real pedestrian density. In addition, future research will benefit from video-based data collection systems around the stadium to better characterize arrival patterns, velocity profiles, and the spatial distribution of pedestrians across adjacent streets, as well as to validate simulation's path-finding algorithms and improved crowd models. Moreover, the implementation of the queuing mechanism, combined with the limited capability of the SFM to reproduce bidirectional pedestrian flows beyond moderately dense conditions, presents opportunities for further improvements.

This study advances current understanding of pedestrian ingress in stadiums and other large-venue settings, supporting the development of evidence-based crowd management strategies that can be tested and refined before real-world implementations. Beyond retrospective assessment, the presented approach establishes a flexible framework for exploring "what-if" scenarios, from spatial reconfigurations like fan zones or food truck areas to alternative security and contingency schemes, supporting safer and more adaptive operations, and ultimately more successful large-scale events.

Acknowledgments

This research is supported by the Provincial Council of Bizkaia, Spain under Technology Transfer Program 2023–M^{3}OVE and 2025–DigiCasco and also by the Basque Government, Spain through the BERC 2022–2025 program and by the Ministry of Science and Innovation, Spain: BCAM Severo Ochoa accreditation CEX2021-001142-S/MICIN / AEI/10.13039/501100011033. The authors acknowledge Borja Gonzalez and Athletic Club for providing the turnstile data, and extend their gratitude to Rubén Peña, Andoni Zalaya and June Asua for their support in developing the realistic-looking 3D animations.

Appendix A. Effect of the queuing-related parameters

In our simulations, queuing-related parameters R_q and c_q were selected following our previous study [73], with additional justification provided at the end of Section 2.3.

We recognize that these parameters critically affect simulation outcomes, as prolonged queues can disrupt local mobility around each gate. In order to explore the impact of these parameters, we performed simulations under Protocol 1, as it exhibits moderate congestion and counterflow in the absence of further mobility interventions. By varying R_q in the range $[0.90, 1.60]$ m with 0.05 increments and c_q in $[0.15, 0.30]$ with 0.01 increments, we produce a flow–clog diagram to identify the parameter choices for which bottleneck formation is more likely to occur.

Supplementary material contains two videos that complement the analysis, `SM_flow_phase.gif` and `SM_clog_phase.gif`, respectively. The former shows the free-flow case while the latter illustrates how a clogging event emerges. Blue-colored agents queue at gate 11, purple-colored ones at gate 12, and red-colored agents indicate those pedestrians not forming part of a queue. These videos illustrate the expected crowd behavior under different queuing assumptions.

Fig. 9 shows the flow–clog diagram as a function of the queuing parameters. Here, the identification of clogged or free-flowing state is based solely on a simple visual inspection of the whole ingress process. Here, the criterion to define a system as clogged is when a prolonged interruption in pedestrian movement occurs or the density exceeds the model's capacity (causing the simulation to fail). Note that the parametric choice parameters used in Table 2 fall within the green region, far from values that induce clogging.

Table 4
Spawning-area probabilities for the different simulation settings.

Setting \ Street	Str. 1	Str. 2	Str. 3	Str. 4	Str. 5
Sett. 1	15%	22.5%	20%	20%	22.5%
Sett. 2	10%	30%	15%	15%	30%
Sett. 3	20%	20%	20%	20%	20%
Sett. 4	10%	40%	40%	10%	0%
Sett. 5	0%	10%	10%	40%	40%

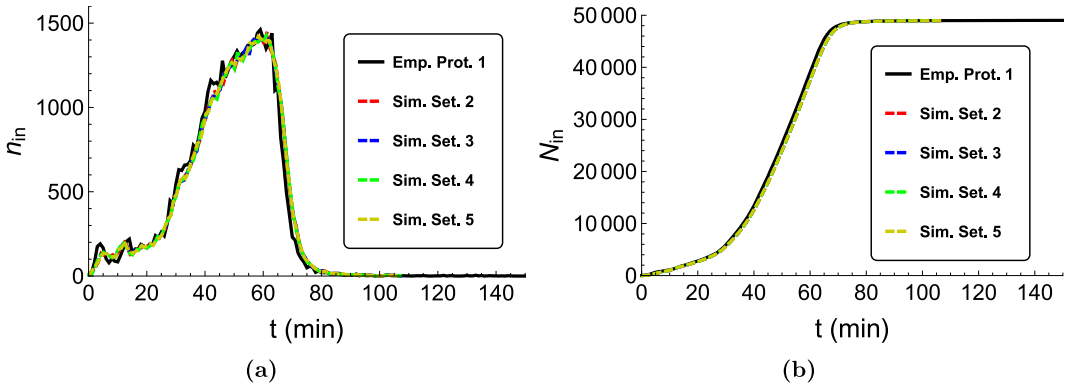

Fig. 10. Empirical (solid lines) and simulated (dashed lines) numbers of fans entering San Mamés Stadium relative to the first arrival time, for Protocol 1 in Table 1 and the new spawning probability configurations listed in Table 4. (a) Distribution of spectator arrivals over time, and (b) its cumulative sum.

A formal definition of clog and flow states, and clogging transition carries deeper significance [83–87]. Further investigation of these theoretical aspects is beyond the scope of this study, which focuses on providing actionable, simulation-informed insights to guide effective crowd management strategies in realistic urban settings.

Appendix B. Sensitivity to spawning-area probability assignments

The probabilities assigned to instantiated pedestrians along their access streets were set based on the reasonable fact that more agents tend to enter via streets connected to the public transport network, as well as from streets where fans typically gather before the match. This arbitrary assignment of probabilities naturally conditions the spatial inflow patterns and may influence simulation outcomes. To assess its impact, we perform an exploratory analysis of how varying the probability assignments to each spawning area would affect the consistency of the results.

Protocol 1 is used as a test case (as in Appendix A), as it is more prone to developing localized congestion and is the only protocol in which all five spawning streets are available. The same simulation settings are maintained, with only the probability assignments adjusted according to Table 4.

For comparison purposes, the probability assignment to each spawning area adopted in the main article is denoted here as Sett. 1. In this appendix, we analyze four additional probability configurations, labeled Sett. 2–5. Settings 2 and 3 introduce minor deviations from Sett. 1 to evaluate the sensitivity of the results to small perturbations: the former slightly higher in Str. 3 and 5, and the latter with evenly distributed probabilities. By contrast, Settings 4 and 5 seek replicate more substantial departures from the baseline case, motivated by hypothetical metro service disruptions that fully redirect pedestrian inflow through alternative streets. Specifically, Sett. 4 assumes closure of the metro exits near Str. 4 and Str. 5, whereas Sett. 5 assumes closure of the exits near Str. 2 and Str. 3.

Consistent with the methodology described in the main article, all reported results in this section correspond to averages over three independent simulation runs.

In Fig. 10, we compare the empirical and numerical access-time distributions and cumulative functions for Settings 2–5. Regardless of the chosen probabilities, the simulated curves fit the empirical data. The absence of long-lasting clogs ensures that agents reach their assigned gates seamlessly, supporting the reliability of the simulation regardless of the specific generation probabilities and explaining the close agreement between modeled and empirical arrival curves.

To compare the averaged local density field resulting from an alternative case (Settings 2–5) with the baseline one (Sett. 1), we compute its relative change from baseline and plot its corresponding heatmap for each case. Let $\langle \rho_s(\mathbf{r}) \rangle$ denote the averaged density field value for a given probability configuration labeled as Sett. s, with $s = \{2, 3, 4, 5\}$ corresponding to the alternative assignments listed in Table 4. We then define the relative change $\langle \rho_{\text{rel}}(\mathbf{r}) \rangle$ of averaged local density with respect to the baseline case $\langle \rho_1(\mathbf{r}) \rangle$ from Sett. 1 as:

$$\langle \rho_{\text{rel}}(\mathbf{r}) \rangle = \frac{\langle \rho_s(\mathbf{r}) \rangle - \langle \rho_1(\mathbf{r}) \rangle}{\langle \rho_1(\mathbf{r}) \rangle}. \tag{B.1}$$

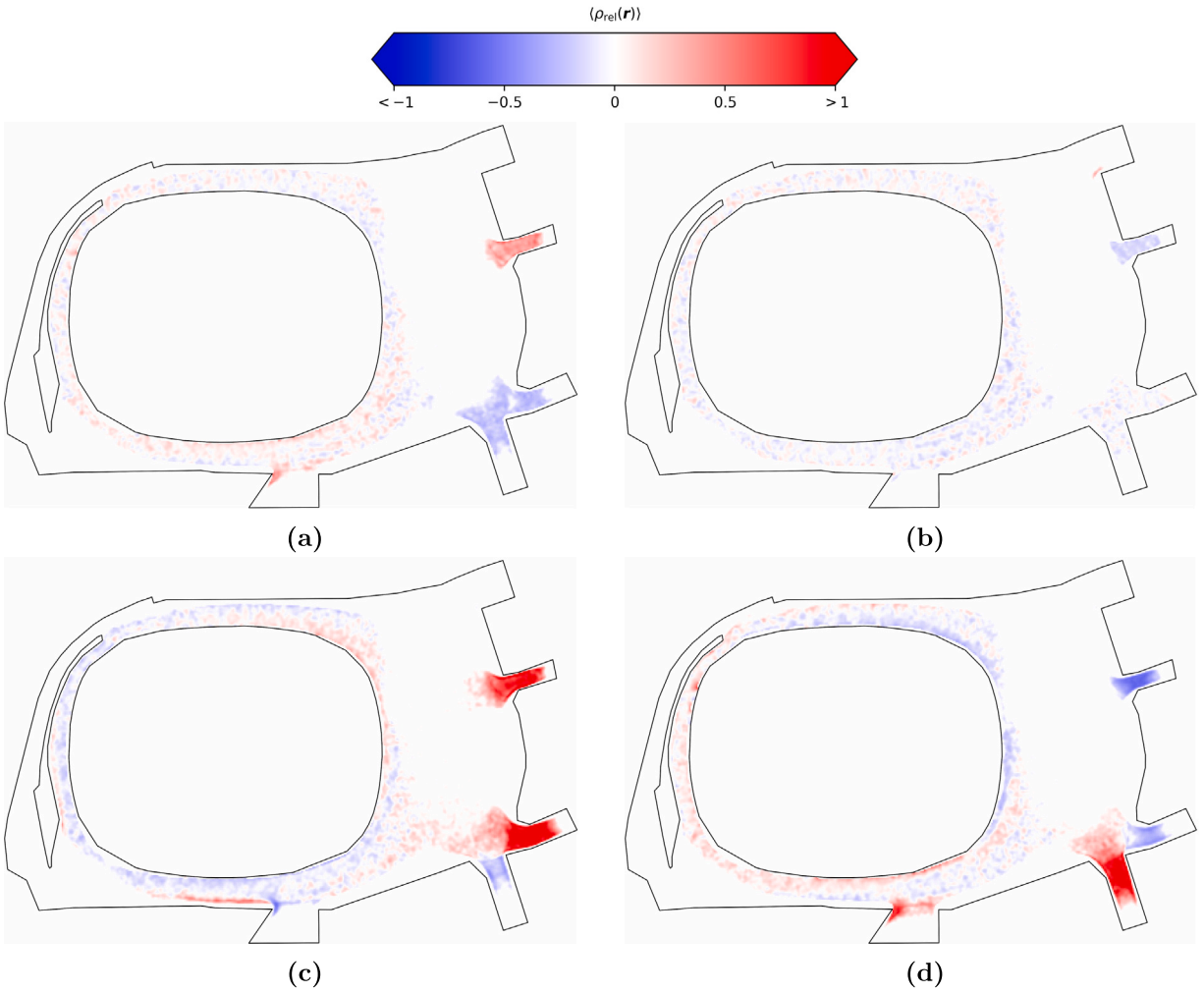

Fig. 11. Relative pedestrian density fields $\langle \rho_{\text{rel}}(\mathbf{r}) \rangle$ in the 15 min with the highest local density in Protocol 1 simulations and settings (a) 2, (b) 3, (c) 4, and (d) 5.

The calculation is performed only for locations where $\langle \rho(\mathbf{r}) \rangle \geq W(0) = 0.1367, \text{person/m}^2$ in order to avoid artificially large relative differences in areas with spurious or null density. This threshold value $W(0)$ corresponds to the self contribution of pedestrians in the density calculation from Eq. (3.2).

Fig. 11 shows the heatmaps relative to the baseline case, $\langle \rho_{\text{rel}}(\mathbf{r}) \rangle$. Settings 2 and 3 exhibit 62% and 33% maximum variations with respect to the baseline case, respectively. These changes are observed primarily near the spawning areas, while densities at the gates and in stadium-adjacent zones remain largely unchanged, highlighting the localized impact of inflow modifications.

Settings 4 and 5 display larger differences. The spawning areas reserved for 40% of the inflow show more than twice the local density (139% in Sett. 4 and 130% in Sett. 5) compared to the baseline, due to the high concentration of the inflow. This difference is larger in zones close to narrow streets (2, 3, and 4) compared to wider ones (Str. 5). For Sett. 4, the relative density raises up to a 38% near gates 17–24, with slight reductions in the remaining stadium-adjacent zones. Finally, Sett. 5 exhibits the highest local density increment beside the stadium, reaching a maximum of 73% increase next to gate 12. With Str. 4 and Str. 5 being busiest streets, a larger pedestrian flow is concentrated in the narrow area beside the North Grandstand, leading to higher $\langle \rho_{\text{rel}}(\mathbf{r}) \rangle$ values.

The results presented in this appendix indicate that, even under the same management protocol, spatial flow patterns are sensitive to pedestrians' probability assignments (i.e., their chosen access routes) as they define a stochastic initial conditions, while the robustness of entry-time statistics underscores the model's reliability for probing overall crowd dynamics under alternative scenarios.

Appendix C. Supplementary data

Supplementary material related to this article can be found online at https://doi.org/10.1016/j.simpat.2026.103279.

Data availability

The data that has been used is confidential.

References

[1] C. Martella, J. Li, C. Conrado, A. Vermeeren, On current crowd management practices and the need for increased situation awareness, prediction, and intervention, Saf. Sci. 91 (2017) 381–393, http://dx.doi.org/10.1016/j.ssci.2016.09.006, URL https://www.sciencedirect.com/science/article/pii/S0925753516302089.

[2] C. Feliciani, A. Corbetta, M. Haghani, K. Nishinari, Trends in crowd accidents based on an analysis of press reports, Saf. Sci. 164 (2023) 106174, http://dx.doi.org/10.1016/j.ssci.2023.106174, URL https://www.sciencedirect.com/science/article/pii/S0925753523001169.

[3] J. Bucks, The Hajj crush: 'It was the closest thing to hell on Earth, 2015, https://www.theguardian.com/news/2015/dec/23/hajj-crush-pilgrimage-mecca-stampede-saudi-arabia-mina-valley. Online; (Accessed 15 August 2023).

[4] H. Gold, Crush at religious festival in Israel's Mount Meron kills 45 people, 2021, https://edition.cnn.com/2021/04/29/world/israel-stampede-intl. Online; (Accessed 12 May 2025).

[5] S. Hrishikesh, More than 120 killed in crush at India religious event, 2024, https://www.bbc.com/news/articles/cv2g7wgj83no. Online; (Accessed 12 May 2025).

[6] How joy turned to horror as Kumbh Mela festival crowd crush unfolded, 2025, https://www.theguardian.com/world/2025/jan/30/kumbh-mela-festival-crowd-crush-india. Online; (Accessed 12 May 2025).

[7] Love parade deaths: 10 charged over crush at festival, 2014, https://www.bbc.com/news/world-europe-26152045. Online; (Accessed 12 May 2025).

[8] Astroworld: deaths of 10 people at Houston concert ruled accidental, 2021, https://www.theguardian.com/music/2021/dec/16/astroworld-festival-deaths-ruled-accidental. Online; (Accessed 12 May 2025).

[9] B. García Gallo, Trial over Madrid Arena Halloween party deaths gets underway, 2016, https://english.elpais.com/elpais/2016/01/14/inenglish/1452784245_664113.html. Online; (Accessed 12 May 2025).

[10] J. Yeung, T. Rebane, 'Somebody is going to die': How Seoul's deadly Halloween crush unfolded, 2022, https://edition.cnn.com/2022/11/04/asia/itaewon-seoul-korea-halloween-crush-timeline-intl-hnk-dst/index.html. Online; (Accessed 15 August 2023).

[11] T. Mullen, Heysel disaster: English football's forgotten tragedy?, 2015, https://www.bbc.com/news/uk-england-merseyside-32898612. Online; (Accessed 15 August 2023).

[12] Hillsborough: Timeline of the 1989 stadium disaster, 2022, https://www.bbc.com/news/uk-england-merseyside-47697569. Online; (Accessed 15 August 2023).

[13] F. Mao, Indonesia football crush: How the disaster unfolded, 2022, https://www.bbc.com/news/world-asia-63113027. Online; (Accessed 15 August 2023).

[14] El Salvador stadium crush leaves at least twelve dead, 2023, https://www.bbc.com/news/world-latin-america-65662194. Online; (Accessed 15 August 2023).

[15] At least 56 people killed in crush at Guinea football stadium, 2024, https://www.theguardian.com/world/2024/dec/02/crowd-crush-football-stadium-nzerekore-guinea. Online; (Accessed 12 May 2025).

[16] D. Conn, Uefa had 'primary responsibility' for Champions League final chaos, damning report finds, 2023, https://www.theguardian.com/football/2023/feb/13/champions-league-final-report-uefa-primary-responsibility-chaos-paris-liverpool-real-madrid. Online; (Accessed 15 August 2023).

[17] B. Hankin, R. Wright, Passenger flow in subways, J. Oper. Res. Soc. - J. Oper. Res. Soc. 9 (1958) 81–88, http://dx.doi.org/10.1057/jors.1958.9.

[18] J. Zhang, W. Klingsch, A. Schadschneider, A. Seyfried, Transitions in pedestrian fundamental diagrams of straight corridors and T-junctions, J. Stat. Mech. Theory Exp. 2011 (2011) P06004, http://dx.doi.org/10.1088/1742-5468/2011/06/P06004.

[19] S. Older, Movement of pedestrians on footways in shopping streets, Traffic Eng. Contr. 10 (1967).

[20] M. Mōri, H. Tsukaguchi, A new method for evaluation of level of service in pedestrian facilities, Transp. Res. Part A: Gen. 21 (1987) 223–234, http://dx.doi.org/10.1016/0191-2607(87)90016-1.

[21] U. Weidmann, Transporttechnik der fussgänger, Schriftenr. Inst. Verk. Transp. Straen- Eisenb. 78 (1993) 62–64.

[22] K. Müller, Zur Gestaltung und Bemessung von Fluchtwegen für die Evakuierung von Personen aus Bauwerken auf der Grundlage von Modellversuchen. Dissertation, Technische Hochschule Magdeburg, 1981.

[23] X. Liu, W. Song, W. Lv, Empirical data for pedestrian counterflow through bottlenecks in the channel, Transp. Res. Procedia 2 (2014) http://dx.doi.org/10.1016/j.trpro.2014.09.006.

[24] T. Kretz, A. Grünebohm, M. Schreckenberg, Experimental study of pedestrian flow through a bottleneck, J. Stat. Mech. Theory Exp. (2006) P10014, http://dx.doi.org/10.1088/1742-5468/2006/10/P10014.

[25] A. Seyfried, O. Passon, B. Steffen, M. Boltes, T. Rupprecht, W. Klingsch, New insights into pedestrian flow through bottlenecks, Transp. Sci. 43 (2007) 395–406, http://dx.doi.org/10.1287/trsc.1090.0263.

[26] R. Nagai, M. Fukamachi, T. Nagatani, Evacuation of crawlers and walkers from corridor through an exit, Phys. A-Stat. Mech. Appl. - Physica A 367 (2006) 449–460, http://dx.doi.org/10.1016/j.physa.2005.11.031.

[27] H. Muir, D. Bottomley, C. Marrison, Effects of motivation and cabin configuration on emergency aircraft evacuation behavior and rates of egress, Int. J. Aviat. Psychol. - Int. J. Aviat. Psychol. 6 (1996) 57–77, http://dx.doi.org/10.1207/s15327108ijap0601_4.

[28] T. Rupprecht, W. Klingsch, A. Seyfried, Influence of geometry parameters on pedestrian flow through bottleneck, in: Proc. 5th Int. Conf. Pedestrian Evac. Dynam., Springer, 2011, http://dx.doi.org/10.1007/978-1-4419-9725-8_7.

[29] W. Liao, A. Seyfried, J. Zhang, M. Boltes, Z. Xiaoping, Y. Zhao, Experimental study on pedestrian flow through wide bottleneck, Transp. Res. Procedia 2 (2014) 26–33, http://dx.doi.org/10.1016/j.trpro.2014.09.005, The Conference on Pedestrian and Evacuation Dynamics 2014 (PED 2014), 22-24 October 2014, Delft, The Netherlands.

[30] A. Sieben, J. Schumann, A. Seyfried, Collective phenomena in crowds—Where pedestrian dynamics need social psychology, PLoS One 12 (2017) http://dx.doi.org/10.1371/journal.pone.0177328.

[31] J. Adrian, M. Boltes, S. Holl, A. Sieben, A. Seyfried, Crowding and queuing in entrance scenarios: Influence of corridor width in front of bottlenecks, Collect. Dyn. 5 (2020) http://dx.doi.org/10.17815/CD.2020.50.

[32] E. Üsten, H. Lügering, A. Sieben, Pushing and non-pushing forward motion in crowds: A systematic psychological observation method for rating individual behavior in pedestrian dynamics, Collect. Dyn. 7 (2022) 1–16, http://dx.doi.org/10.17815/CD.2022.138.

[33] E. Üsten, A. Sieben, Don't stop me now: Psychological effects of interrupting a moving pedestrian crowd and a video game, PLoS One 18 (2023) e0287583, http://dx.doi.org/10.1371/journal.pone.0287583.

[34] F. He, J. Yue, J. Zhu, A. Seyfried, D. Casas, J. Pettré, H. Wang, Learning extremely high density crowds as active matters, 2025, arXiv:2503.12168. URL https://arxiv.org/abs/2503.12168. arXiv:2503.12168 [cs.CV].

[35] F. Gu, B. Guiselin, N. Bain, I. Zuriguel, D. Bartolo, Emergence of collective oscillations in massive human crowds, Nature 638 (2025) 112–119, http://dx.doi.org/10.1038/s41586-024-08514-6.

[36] D. Helbing, P. Molnár, Social force model for pedestrian dynamics, Phys. Rev. E 51 (1995) 4282–4286, http://dx.doi.org/10.1103/PhysRevE.51.4282, URL https://link.aps.org/doi/10.1103/PhysRevE.51.4282.

[37] A. García, D. Hernández-Delfin, D.-J. Lee, M. Ellero, Limited visual range in the social force model: Effects on macroscopic and microscopic dynamics, Phys. A 612 (2023) 128461, http://dx.doi.org/10.1016/j.physa.2023.128461.

[38] M. Chraibi, A. Seyfried, A. Schadschneider, Generalized centrifugal force model for pedestrian dynamics, Phys. Rev. E Stat. Nonlinear Soft Matter Phys. 82 (2010) 046111, http://dx.doi.org/10.1103/PhysRevE.82.046111.

[39] Y. Wang, J. Ge, A. Comber, An agent-based simulation model of pedestrian evacuation based on Bayesian Nash equilibrium, J. Artif. Soc. Soc. Simul. 26 (3) (2023) 6.

[40] A. Tordeux, M. Chraibi, A. Seyfried, Collision-free speed model for pedestrian dynamics, 2016, pp. 225–232, http://dx.doi.org/10.1007/978-3-319-33482-0_29.

[41] Q. Xu, M. Chraibi, A. Seyfried, Anticipation in a velocity-based model for pedestrian dynamics, Transp. Res. Part C: Emerg. Technol. 133 (2021) 103464, http://dx.doi.org/10.1016/j.trc.2021.103464.

[42] Q. Xu, Z. Yuan, R. Guo, B. He, M. Chraibi, Analysis and modeling of detours in pedestrian operational navigation, Transp. Res. Part C: Emerg. Technol. 162 (2024) 104584, http://dx.doi.org/10.1016/j.trc.2024.104584.

[43] R.L. Hughes, A continuum theory for the flow of pedestrians, Transp. Res. Part B: Methodol. 36 (6) (2002) 507–535, http://dx.doi.org/10.1016/S0191-2615(01)00015-7, URL https://www.sciencedirect.com/science/article/pii/S0191261501000157.

[44] I. Karamouzas, B. Skinner, S. Guy, Universal power law governing pedestrian interactions, Phys. Rev. Lett. 113 (2014) http://dx.doi.org/10.1103/PhysRevLett.113.238701.

[45] I. Echeverria, A. Nicolas, Body and mind: Decoding the dynamics of pedestrians and the effect of smartphone distraction by coupling mechanical and decisional processes, Transp. Res. Part C Emerg. Technol. 157 (2023) 104365, http://dx.doi.org/10.1016/j.trc.2023.104365.

[46] V. Blue, J. Adler, Emergent fundamental pedestrian flows from cellular automata microsimulation, Transp. Res. Rec. 1644 (1998) 29–36, http://dx.doi.org/10.3141/1644-04.

[47] C. Burstedde, K. Klauck, A. Schadschneider, J. Zittartz, Simulation of pedestrian dynamics using a two-dimensional cellular automaton, Phys. A 295 (2001) 507–525, http://dx.doi.org/10.1016/S0378-4371(01)00141-8.

[48] H. Wang, W. Zhi, G. Batista, R. Chandra, Pedestrian trajectory prediction using goal-driven and dynamics-based deep learning framework, Expert Syst. Appl. 271 (2025) 126557, http://dx.doi.org/10.1016/j.eswa.2025.126557, URL https://www.sciencedirect.com/science/article/pii/S0957417425001794.

[49] F. Chen, Q. Zhao, M. Cao, J. Chen, G. Fu, Adaptive agent-based modeling framework for collective decision-making in crowd building evacuation, J. Shanghai Jiaotong Univ. (Sci.) 26 (4) (2021) 522–533, http://dx.doi.org/10.1007/s12204-021-2287-3.

[50] G.P.D.P. Senanayake, M. Kieu, Y. Zou, K. Dirks, Agent-based simulation for pedestrian evacuation: A systematic literature review, Int. J. Disaster Risk Reduct. 111 (2024) 104705, http://dx.doi.org/10.1016/j.ijdrr.2024.104705, URL https://www.sciencedirect.com/science/article/pii/S2212420924004679.

[51] D. Duives, W. Daamen, S. Hoogendoorn, State-of-the-art crowd motion simulation models, Transp. Res. Part C: Emerg. Technol. 37 (2013) 193–209, http://dx.doi.org/10.1016/j.trc.2013.02.005.

[52] M. Haghani, Empirical methods in pedestrian, crowd and evacuation dynamics: Part I. experimental methods and emerging topics, Saf. Sci. 129 (2020) 104743, http://dx.doi.org/10.1016/j.ssci.2020.104743, URL https://www.sciencedirect.com/science/article/pii/S0925753520301405.

[53] S. Yang, T. Li, X. Gong, B. Peng, J. Hu, A review on crowd simulation and modeling, Graph. Model. 111 (2020) 101081, http://dx.doi.org/10.1016/j.gmod.2020.101081, URL https://www.sciencedirect.com/science/article/pii/S1524070320300242.

[54] A. Corbetta, F. Toschi, Physics of human crowds, Annu. Rev. Condens. Matter Phys. 14 (2023) 311–333, http://dx.doi.org/10.1146/annurev-conmatphys-031620-100450.

[55] H.-T. Dang, B. Gaudou, N. Verstaevel, A literature review of dense crowd simulation, Simul. Model. Pr. Theory 134 (2024) 102955, http://dx.doi.org/10.1016/j.simpat.2024.102955, URL https://www.sciencedirect.com/science/article/pii/S1569190X24000698.

[56] J. Gales, K. Chin, T. Young, E. Carattin, M.-Y. Man Oram, Introduction to pedestrian movement and behaviour in stadia, in: J. Gales, K. Chin, T. Young, E. Carattin, M.-Y. Man Oram (Eds.), Egress Modelling of Pedestrians for the Design of Contemporary Stadia, Springer Nature Switzerland, Cham, 2023, pp. 1–28, http://dx.doi.org/10.1007/978-3-031-33472-6_1.

[57] H. Klüpfel, T. Meyer-König, Simulation of the evacuation of a football stadium using the CA model PedGo, 2005, pp. 423–428, http://dx.doi.org/10.1007/3-540-28091-X_43.

[58] A. Tsiftsis, I. Georgoudas, G. Sirakoulis, Real data evaluation of a crowd supervising system for stadium evacuation and its hardware implementation, IEEE Syst. J. 10 (2015) 1–12, http://dx.doi.org/10.1109/JSYST.2014.2370455.

[59] Y. Dong, X. Jia, D. Yanagisawa, K. Nishinari, Optimising pedestrian flow around large stadiums, Collect. Dyn. 6 (2021) http://dx.doi.org/10.17815/CD.2021.117.

[60] C.-H. Yang, C.-Y. Lin, T.-W. Kuo, Simulation-based assessment of evacuation efficiency in sports stadiums: Insights from case studies, Fire 8 (6) (2025) 210, http://dx.doi.org/10.3390/fire8060210, URL https://www.mdpi.com/2571-6255/8/6/210.

[61] M. Gravit, E. Kirik, E. Savchenko, T. Vitova, D. Shabunina, Simulation of evacuation from stadiums and entertainment arenas of different epochs on the example of the Roman Colosseum and the Gazprom Arena, Fire 5 (2022) 20, http://dx.doi.org/10.3390/fire5010020.

[62] Z. Fang, Q. Li, Q. Li, L. Han, D. Wang, A proposed pedestrian waiting-time model for improving space–time use efficiency in stadium evacuation scenarios, Build. Environ. 46 (2011) 1774–1784, http://dx.doi.org/10.1016/j.buildenv.2011.02.005.

[63] K. Chin, T. Young, B. Chorlton, D. Aucoin, J. Gales, Crowd behaviour in Canadian football stadia - part 1 - data collection, Can. J. Civ. Eng. 49 (2021) http://dx.doi.org/10.1139/cjce-2021-0425.

[64] A. García, D. Hernández-Delfin, B. González, G. Garitaonaindia, D.-J. Lee, M. Ellero, Analysis of local density during football stadium access: Integrating pedestrian flow simulations and empirical data, Phys. A 638 (2024) 129635, http://dx.doi.org/10.1016/j.physa.2024.129635.

[65] Athletic Club, https://es.uefa.com/uefaeuropaleague/news/0283-186939a1c517-e1cf7c66cc8e-1000–2025-uefa-europa-league-final-venue-san-mames/. Online; (Accessed 8 April 2025).

[66] Athletic Club, https://www.bilbaoturismo.net/BilbaoTurismo/en/big-events/bilbao-finals-2018_2. Online; (Accessed 8 April 2025).

[67] Athletic Club, https://www.uefa.com/womenschampionsleague/news/0282-182b080b479e-f1bfbaaf9167-1000–2024-uefa-women-s-champions-league-final-bilbao/. Online; (Accessed 8 April 2025).

[68] Athletic Club, https://sanmames.athletic-club.eus/en/blog/san-mames-to-host-european-rugby-champions-cup-final-in-2026/. Online; (Accessed 8 April 2025).

[69] https://www.deia.eus/athletic/2024/12/11/fifa-oficial-san-mames-sera-9038449.html. (Accessed 28 October 2025).

[70] https://www.athletic-club.eus/en/news/2025/04/16/instructions-for-entering-san-mames-before-athletic-vs-rangers/. (Accessed 28 October 2025).

[71] https://www.athletic-club.eus/en/news/2025/04/29/instructions-for-entering-san-mames-before-athletic-vs-manchester-united/. (Accessed 28 October 2025).

[72] S. Osorio, Así será el acceso a san mamés de las aficiones en la final de la europa league: nuevo filtro de seguridad en sabino arana y recorridos diferentes, 2025, https://www.elcorreo.com/bizkaia/acceso-san-mames-aficiones-final-europa-league-20250514131254-nt.html. Online; (Accessed 29 May 2025).

[73] A. García, D. Hernández-Delfin, D.-J. Lee, M. Ellero, On the modeling of dynamic queue formation and decision-making in pedestrian dynamics simulations, Simul. Model. Pr. Theory 142 (2025) 103130, http://dx.doi.org/10.1016/j.simpat.2025.103130.

[74] D. Helbing, I. Farkas, T. Vicsek, Simulating dynamic features of escape panic, Nature 407 (2000) 487–490, http://dx.doi.org/10.1038/35035023.
[75] D. Helbing, A. Johansson, Pedestrian, crowd and evacuation dynamics, 16, 2010, pp. 697–716, http://dx.doi.org/10.1007/978-1-4419-7695-6_37,
[76] E. Cristiani, B. Piccoli, A. Tosin, Multiscale Modeling of Pedestrian Dynamics, vol. 12, Springer, 2014, pp. 112–113, http://dx.doi.org/10.1007/978-3-319-06620-2.
[77] B. Steffen, A. Seyfried, Methods for measuring pedestrian density, flow, speed and direction with minimal scatter, Phys. A 389 (9) (2010) 1902–1910, http://dx.doi.org/10.1016/j.physa.2009.12.015, URL https://www.sciencedirect.com/science/article/pii/S0378437109010115.
[78] D.C. Duives, W. Daamen, S.P. Hoogendoorn, Quantification of the level of crowdedness for pedestrian movements, Phys. A 427 (2015) 162–180, http://dx.doi.org/10.1016/j.physa.2014.11.054, URL https://www.sciencedirect.com/science/article/pii/S0378437114010164.
[79] M. Ellero, N.A. Adams, SPH simulations of flow around a periodic array of cylinders confined in a channel, Internat. J. Numer. Methods Engrg. 86 (8) (2011) 1027–1040, http://dx.doi.org/10.1002/nme.3088, URL https://onlinelibrary.wiley.com/doi/10.1002/nme.3088.
[80] M. Liu, G. Liu, K. Lam, Constructing smoothing functions in smoothed particle hydrodynamics with applications, J. Comput. Appl. Math. 155 (2003) 263–284, http://dx.doi.org/10.1016/S0377-0427(02)00869-5.
[81] D. Oberhagemann, Static and Dynamic Crowd Densities at Major Public Events, Technical Report tb 13-01, Vereinigung zur Förderung des Deutschen Brandschutzes e. V. (vfdb), Altenberge; Lippetal, Germany, 2012, URL https://www.vfdb.de/media/doc/sonstiges/forschung/eva/tb_13_01_crowd_densities.pdf.
[82] A.S. Diario, Live recording of the pre-game security screening at the UEFA Europa League final, 2025, https://www.youtube.com/live/rGWV5wH7Lac?t=1769s. (Accessed 19 February 2026).
[83] I. Zuriguel, D.R. Parisi, R.C. Hidalgo, C. Lozano, A. Janda, P.A. Gago, J.P. Peralta, L.M. Ferrer, L.A. Pugnaloni, E. Clément, D. Maza, I. Pagonabarraga, A. Garcimartín, Clogging transition of many-particle systems flowing through bottlenecks, Sci. Rep. 4 (1) (2014) 7324, http://dx.doi.org/10.1038/srep07324, URL https://www.nature.com/articles/srep07324.
[84] R. Caitano, B.V. Guerrero, R.E.R. González, I. Zuriguel, A. Garcimartín, Characterization of the clogging transition in vibrated granular media, Phys. Rev. Lett. 127 (2021) 148002, http://dx.doi.org/10.1103/PhysRevLett.127.148002, URL https://link.aps.org/doi/10.1103/PhysRevLett.127.148002.
[85] Y. Tajima, K. Takimoto, T. Nagatani, Pattern formation and jamming transition in pedestrian counter flow, Phys. A 313 (3) (2002) 709–723, http://dx.doi.org/10.1016/S0378-4371(02)00965-2, URL https://www.sciencedirect.com/science/article/pii/S0378437102009652.
[86] Q. Xu, M. Chraibi, A. Seyfried, Prolonged clogs in bottleneck simulations for pedestrian dynamics, Phys. A 573 (2021) 125934, http://dx.doi.org/10.1016/j.physa.2021.125934, URL https://www.sciencedirect.com/science/article/pii/S0378437121002065.
[87] D. Hernández-Delfin, A. García, M. Ellero, Rheology of a crowd: From faster-is-slower to shear thickening, Commun. Phys. 7 (1) (2024) 152, http://dx.doi.org/10.1038/s42005-024-01646-1, URL https://www.nature.com/articles/s42005-024-01646-1.